PCCP
Physical Chemistry Chemical Physics

Accepted Manuscript

This article can be cited before page numbers have been issued, to do this please use: H. A. Roy and M. Rodgers, *Phys. Chem. Chem. Phys.*, 2021, DOI: 10.1039/D1CP02928B.

ROYAL SOCIETY OF CHEMISTRY

rsc.li/pccp

View Article Online
DOI: 10.1039/D1CP02928B

submtted to Phys. Chem. Chem. Phys.

1-Alkyl-3-Methylimidazolium Cation Binding Preferences in Hexafluorophosphate Ionic Liquid Clusters Determined Using Competitive TCID Measurements and Theoretical Calculations

H. A. Roy and M. T. Rodgers*

Department of Chemistry, Wayne State University, Detroit, MI, 48202, USA

ABSTRACT:

Ionic liquids (ILs) exhibit unique properties that have led to their development and widespread use for a variety of applications. Development efforts have generally focused on achieving desired macroscopic properties via tuning of the IL through variation of the cations and anions. Both the macroscopic and microscopic properties of an IL influence its tunability and thus feasibility of use for selected applications. Works geared toward a microscopic understanding of the nature and strength of the intrinsic cation-anion interactions of ILs have been limited to date. Specifically, the intrinsic strength of the cation-anion interactions in ILs is largely unknown. In previous work, we employed threshold collision-induced dissociation (TCID) approaches supported and enhanced by electronic structure calculations to determine the bond dissociation energies (BDEs) and characterize the nature of the cation-anion interactions in a series of four 2:1 clusters of 1-alkyl-3-methylimidazolium cations with the hexafluorophosphate anion, $[2C_n\text{mim:PF}_6]^+$. To examine the effects of the 1-alkyl chain on the structure and energetics of binding, the cation was varied over the series: 1-ethyl-3-methylimidazolium, $[C_2\text{mim}]^+$, 1-butyl-3-methylimidazolium, $[C_4\text{mim}]^+$, 1-hexyl-3-methylimidazolium, $[C_6\text{mim}]^+$, and 1-octyl-3-methylimidazolium, $[C_8\text{mim}]^+$. The variation in the strength of binding among these $[2C_n\text{mim:PF}_6]^+$ clusters was found to be similar in magnitude to the average experimental uncertainty in the measurements. To definitively establish an absolute order of binding among these $[2C_n\text{mim:PF}_6]^+$ clusters, we extend this work again using TCID and electronic structure theory approaches to include competitive binding studies of three mixed 2:1 clusters of 1-alkyl-3-methylimidazolium cations and the hexafluorophosphate anion, $[C_{n-2}\text{mim:PF}_6\text{:}C_n\text{mim}]^+$ for n = 4, 6, and 8. The absolute BDEs of these mixed $[C_{n-2}\text{mim:PF}_6\text{:}C_n\text{mim}]^+$ clusters as well as the absolute difference in the strength of the intrinsic binding interactions as a function of the cation are determined with significantly improved precision. By combining the thermochemical results of the previous independent and present competitive measurements, the BDEs of the $[2C_n\text{mim:PF}_6]^+$ clusters are both more accurately and more precisely determined. Comparisons are made to results for the analogous $[2C_n\text{mim:BF}_4]^+$ and $[C_{n-2}\text{mim:BF}_4\text{:}C_n\text{mim}]^+$ clusters previously examined to elucidate the effects of the $[PF_6]^-$ and $[BF_4]^-$ anions on the binding.

Corresponding author: M. T. Rodgers, mrodgers@chem.wayne.edu, Tel. (313) 577-2431

View Article Online
DOI: 10.1039/D1CP02928B

INTRODUCTION

Ionic liquids (ILs) are molten salts that typically exhibit melting points below 100° C, much lower than those of traditional salts. The combinatorial diversity of cations and anions that may comprise an IL[1] enable broad tunability of its properties for applications that span the fields of electrochemistry,[2,3] energy storage,[4-6] gas and liquid chromatographic separations,[7-10] organic and inorganic synthesis,[11-13] and space propulsion.[14-16] A thorough understanding of how specific cations and anions influence the properties of an IL is essential to the rational design of ILs for targeted applications. The IL clusters examined in this study are mixed 2:1 complexes of 1-alkyl-3-methylimidazolium cations, designated as $[C_n\text{mim}]^+$ where n = 2, 4, 6 and 8 and indicates the number of carbon atoms in the 1-alkyl chain and the hexafluorophosphate anion, $[PF_6]^-$. The structures of the $[C_n\text{mim}]^+$ cations and $[PF_6]^-$ anion are displayed in **Figure 1**.

Understanding the intrinsic interactions, clustering, and dissociation energetics of ILs for their use as fuels in electrospray propulsion provides the motivation for this work. Specifically, we are interested in characterizing the influence that the cations and anions of an IL have on thrust and efficiency for electrospray propulsion. Knowledge of the gas-phase dissociation dynamics of ILs will aid in the elucidation of that knowledge and help lead the development of task-specific ILs for various applications, and in particular electrospray propulsion. Electrospray propulsion has the advantages of easy miniaturization and low complexity making this technique amenable to nanosatellite propulsion.[17] The propulsion mechanism associated with electrospray thrusters parallels that of electrospray ionization (ESI),[18] presently one of the most commonly employed ionization techniques for mass spectrometry. As in ESI, a high voltage is applied to an electrospray thruster emitter to facilitate the formation of ions. The ions are accelerated in the electric field, generating thrust as the ions are emitted from the spacecraft. The thrust generated is very small such that an array of emitters is needed to generate the required thrust of a small nanosatellite.[17] A variety of ILs are being investigated as greener fuels for space propulsion using electrospray thrusters including imidazolium-based ILs[19-22] and protic ILs.[23,24] The propellant employed for the recent NASA/ESA LISA Pathfinder mission was

View Article Online
DOI: 10.1039/D1CP02928B

1-ethyl-3-methylimidazolium bis(trifluoromethylsulfonyl)imide, C_2mim–Tf_2N.[21,22] A perspective describing the role of mass spectrometry in understanding electrospray thrusters and their plumes has recently been published.[17]

The popularity of ILs for a variety of applications has motivated theoretical and experimental studies aimed at understanding the gas-phase structures, energetics, and reactivity of ILs and their clusters. In particular, electrospray ionization tandem mass spectrometry (ESI-MS/MS) approaches typically using collisional activation have been employed to examine the dissociation behavior of IL clusters and to establish cation-anion interaction scales for ILs.[25-32] These studies have examined the variable-energy CID behavior of cationic and anionic clusters of various ILs as a function of collision energy. In contrast to the threshold CID approach employed here, where energetic information is extracted at the onset of dissociation, these studies were based on comparisons at 50% dissociation. Bini et al. used the variable-energy CID approach to examine the competitive dissociation of $[C_2mim:Br:C_nmim]^+$ clusters for n = 4, 6, and 8. Based on the observed branching ratios, the relative order of binding was found to be $[C_nmim]^+ < [C_2mim]^+$ for all three mixed clusters. Although no other mixed clusters were examined, the trend in relative intensities of the $[C_nmim]^+$ vs. $[C_2mim]^+$ cations observed in these experiments suggest that the relative intrinsic binding for the 1-alkyl-3-methylimidazolium cations to $[Br]^-$ follows the order: $[C_8mim]^+ < [C_6mim]^+ < [C_4mim]^+ < [C_2mim]^+$.[26] The variable-energy CID behavior approach was also used by Fernandes et al. to examine the intrinsic binding of the $[C_nmim]^+$ cations in $[2C_nmim:X]^+$ clusters in which $[X]^- = [Cl]^-$, $[BF_4]^-$, and $[Tf_2N]^-$.[25,29] Based on the center-of-mass collision energies at 50% dissociation, the binding to both $[Cl]^-$ and $[Tf_2N]^-$ follows the order: $[C_8mim]^+ < [C_6mim]^+ < [C_4mim]^+ < [C_2mim]^+$. The same order of binding, $[C_8mim]^+ < [C_4mim]^+ < [C_2mim]^+$was also determined for $[BF_4]^-$; the $[C_6mim]^+$ cation was not included in that work. Vitorino et al.[28] confirmed the relative order of binding of the $[C_nmim]^+$ cations to $[Tf_2N]^-$ as $[C_6mim]^+ < [C_4mim]^+ < [C_2mim]^+$ using Cook's Kinetic method. Given the findings in these earlier works and the structural similarities and differences among the anions examined, an overall relative order of binding of the $[C_nmim]^+$

View Article Online
DOI: 10.1039/D1CP02928B

cations to $[BF_4]^-$ of $[C_8mim]^+ < [C_6mim]^+ < [C_4mim]^+ < [C_2mim]^+$ was anticipated, and similarly for $[PF_6]^-$ even though this anion had not been included in that work. However, because the competitive experiments did not comprehensively examine other mixed clusters, and the energy-resolved experiments did not incorporate internal energy and unimolecular dissociation rates into the comparisons of the experimental data, this supposition was uncertain for $[BF_4]^-$, and remains uncertain for $[PF_6]^-$. Further, these other works have not provided absolute binding affinities or BDEs of the IL clusters under investigation.

The structure of ILs and their clusters have been studied in both the condensed and gas phases using a variety of experimental and theoretical techniques. In a review by Hunt et al. hydrogen-bonding interactions in a variety of IL systems were characterized; favorable cation-anion binding interactions to imidazolium cations were reported. Using C_4mim–Cl as a prototypical imidazolium-based IL, they characterized cation-anion binding interactions as front butyl, front methyl, alkyl methyl, side methyl, back, side butyl, and alkyl methyl binding;[33] the nomenclature used in this work was motivated by their findings. Prince et al. used atomistic molecular dynamics simulations to study C_2mim–Tf_2N IL clusters and report structures and theoretical binding energies from QM and MD simulations for $[xC_2mim:(x\text{-}1)Tf_2N]^+$ clusters for x = 4, 3, and 2 in an effort to characterize dissociation of ILs in the electric fields experienced during ESI propulsion.[34] Synergistic computational chemistry and spectroscopy measurements have probed the structures of $C_n$mim–BF_4 and $C_n$mim–PF_6 ILs where n = 2–4.[35-49] In particular, B3LYP/6-311+G(2d,p) calculations reproduce the Raman and infrared spectra of the ($C_n$mim:PF_6) ion pairs, n = 2–4 with high fidelity.[43] Kamalakannan et al. report ($C_n$mim:PF_6) ion pair structures and ion pairing energies for n = 2, 4, 6, and 8 in a theoretical study of ionic liquids binding to Au(111) surfaces.[48] X-ray crystallography has also been used to characterize $C_n$mim–PF_6 crystal structures.[50-53] Notably, Fullet et al. report front, front alkyl, front methyl, and back binding in the (C_2mim:PF_6) ion pair crystal structures.[50] These findings are consistent with other reported crystal structures.[50-53]

View Article Online
DOI: 10.1039/D1CP02928B

In previous work, we employed threshold collision-induced dissociation (TCID) approaches combined with electronic structure calculations to characterize the nature of the cation-anion interactions in and determine the bond dissociation energies (BDEs) of a series of four 2:1 clusters of 1-alkyl-3-methylimidazolium cations and the hexafluorophosphate anion, $[2C_n\text{mim:PF}_6]^+$ for n = 2, 4, 6, and 8.[54] The primary dissociation pathway observed for all four clusters involves loss of a neutral ($C_n\text{mim:PF}_6$) ion pair, as described by **reaction (1)**.

$$[2C_n\text{mim:PF}_6]^+ + \text{Xe} \rightarrow [C_n\text{mim}]^+ + (C_n\text{mim:PF}_6) + \text{Xe} \quad \textbf{(1)}$$

The BDEs of the $[2C_n\text{mim:PF}_6]^+$clusters were determined from statistical thermochemical analyses of the $[C_n\text{mim}]^+$ product cross sections. The differences in the BDEs measured for these clusters are rather small and of similar magnitude to the uncertainties in the measurements. Thus, the absolute trend in the BDEs as a function of the $[C_n\text{mim}]^+$ cation remain indefinite based only on these measurements. Further, while theory is generally able to predict relative trends with high fidelity, minor inconsistencies in the computed trends are also found among the B3LYP, B3LYP-GD3BJ and M06-2X levels of theory investigated. Similar to the measured BDEs, the accuracy of the theoretically predicted values is at least similar to if not larger than the differences in the strength of binding. Competitive measurements are thus needed to establish a definitive order of binding.

In the present work, theory and experiment are synergistically employed to examine the influence of the $[C_n\text{mim}]^+$ cation on the structure and energetics of binding in mixed $[C_{n-2}\text{mim:PF}_6\text{:}C_n\text{mim}]^+$ IL clusters. Threshold collision-induced dissociation (TCID) of three $[C_{n-2}\text{mim:PF}_6\text{:}C_n\text{mim}]^+$ clusters, where n = 4, 6, and 8, is performed with Xe. Absolute BDEs of these clusters are reported, for the binding of the $[C_n\text{mim}]^+$ cation to the ($C_{n-2}\text{mim:PF}_6$) ion pair and for the binding of the $[C_{n-2}\text{mim}]^+$ cation to the ($C_n\text{mim:PF}_6$) ion pair. Relative ion pairing energies (ΔIPEs) of the ($C_{n-2}\text{mim:PF}_6$) and ($C_n\text{mim:PF}_6$) ion pairs are determined from the differences in the BDEs measured for the $[C_{n-2}\text{mim:PF}_6\text{:}C_n\text{mim}]^+$ clusters and compared to theoretical values. In addition, the absolute BDEs previously reported for the $[2C_n\text{mim:PF}_6]^+$ clusters[54] are combined with the ΔBDEs of the $[2C_{n-2}\text{mim:PF}_6\text{:}C_n\text{mim}]^+$ clusters determined here

View Article Online
DOI: 10.1039/D1CP02928B

and subjected to a maximal likelihood analysis to improve the accuracy and precision in the BDEs determined. Comparisons are also made to analogous results for the $[C_{n-2}mim{:}BF_4{:}C_nmim]^+$ and $[2C_nmim{:}BF_4]^+$ clusters previously investigated[55,56] to further elucidate the influence of these anions on the nature and strength of binding.

EXPERIMENTAL AND COMPUTATIONAL METHODS

Sample Preparation. Materials were purchased from commercial vendors and used as received. Only HPLC-grade solvents were used. 1-Ethyl-3-methylimidazolium hexafluorophosphate, $C_2mim–PF_6$, and 1-octyl-3-methylimidazolium bis(trifluoromethylsulfonyl)imide, $C_8mim–TFSI$, were purchased from Alfa Aesar (Haverhill, MA). 1-Butyl-3-methylimidazolium hexafluorophosphate, $C_4mim–PF_6$, and methanol were purchased from Fisher Scientific (Walthan, MA). 1-Hexyl-3-methylimidazolium bis(trifluoromethylsulfonyl)imide, $C_6mim–TFSI$, and water were purchased from Sigma Aldrich (St. Louis, MO). Working solutions with ~0.5 mM of each constituent IL in 50:50 methanol:water (v:v) were prepared by diluting mixtures of the relevant two (or three) ILs, and relying on ion exchange in solution to enable generation of the desired $[C_{n-2}mim{:}PF_6{:}C_nmim]^+$ cluster via electrospray ionization (ESI).

Experimental Procedures. TCID experiments were performed for three $[C_{n-2}mim{:}PF_6{:}C_nmim]^+$ clusters using a custom-built guided ion beam tandem mass spectrometer (GIBMS)[57] coupled to a custom-built ESI source.[58,59] Sample solutions were directly infused using a syringe pump through a 35 gauge stainless steel ESI emitter at a flow rate of ~ 1.2 μL/min. Taylor cone formation enabling stable ion generation was observed at ~ +2 kV. The ESI plume was sampled through a 0.012" diameter limiting orifice. Ions were transferred to the entrance of the mass spectrometer via a capillary inlet resistively heated to ~100°C. Ions exiting the capillary are trapped in the radial direction by an rf ion funnel (IF) and focused and injected into an rf hexapole ion guide (6P). The IF rf is applied 180° out of phase to alternate adjacent ring electrodes at a frequency of 530 kHz and amplitude of 25 $V_{pp,}$ with a 25 V_{dc} gradient applied

View Article Online
DOI: 10.1039/D1CP02928B

across the IF to guide ions into the mass spectrometer. The last two plates of the IF serve as a limiting orifice to throttle the gas load and as an injection lens to focus and inject the ions into the 6P. The 6P spans a differentially pumped chamber at sufficiently high pressure that the ions undergo $> 10^4$ thermalizing collisions. The ion beam is focused into a magnetic sector momentum analyzer for mass selection of the precursor $[C_{n-2}mim:PF_6:C_nmim]^+$ cluster. After mass selection, the precursor ions were slowed to a nominal kinetic energy using an exponential retarder. The precursor ions were then focused into an rf octopole ion guide (8P) that spans a collision cell to which a dc offset is applied that determines the collision energy of the precursor $[C_{n-2}mim:PF_6:C_nmim]^+$ cluster with the collision gas, Xe. Xenon is chosen as the collision gas for its heavy mass and large polarizability, resulting in larger measured CID cross sections.[60-62] Remaining precursor ions and fragment ions traverse the 8P and are focused into a quadrupole mass filter for product mass analysis. Ions are detected with a Daly detector[63] and standard pulse-counting electronics.

Theoretical Calculations. In previous work, theoretical calculations were performed to characterize the structures and stabilities of the $[C_nmim]^+$ and $[PF_6]^-$ ions and their modes of binding in the $(C_nmim:PF_6)$ ion pairs and $[2C_nmim:PF_6]^+$ clusters.[54,55] Parallel theoretical procedures were pursued here to extend these calculations to include characterization of the structures and stabilities of the mixed $[C_{n-2}mim:PF_6:C_nmim]^+$ clusters. To generate candidate structures for the $[C_{n-2}mim:PF_6:C_nmim]^+$ clusters, the 20 most stable structures previously identified for the $[2C_nmim:PF_6]^+$ clusters were selected and used to generate additional candidate structures for the $[C_{n-2}mim:PF_6:C_nmim]^+$ clusters by replacing the terminal ethyl moiety of the 1-alkyl chain of one of the cations by a hydrogen atom.[55] This procedure generated two candidate structures for the mixed IL cluster from each $[2C_nmim:PF_6]^+$ structure, thereby providing 40 unique structures that were subjected to density functional theory calculations. Electronic structure calculations were performed using the Gaussian 09 suite of programs.[64] Geometry optimizations and frequency analyses were performed using three density function theory methods: B3LYP,[65-68] B3LYP-GD3BJ,[69] and M06-2X[70] each with the triple zeta

View Article Online
DOI: 10.1039/D1CP02928B

6-311+G(d,p) basis set. B3LYP was employed as it is the most commonly used density functional and its strengths and limitations are probably best known. B3LYP-GD3BJ was also examined as B3LYP does not include dispersion and dispersion interactions are likely to be important contributors to the binding in the ($C_n$mim:PF_6) ion pairs and [C_{n-2}mim:PF_6:$C_n$mim]$^+$ clusters as well as to the folding of the 1-alkyl chains of the [$C_n$mim]$^+$ cations. To improve accuracy of the energetic predictions, single point energies were calculated using the same density functional model, but with an extended basis set that includes additional diffuse and polarization functions, the 6-311+G(2d,2p) basis set. Zero-point energy (ZPE) corrections were included for all species and all three levels of theory, while basis set superposition error (BSSE)[71,72] corrections were included in the computed BDEs. To facilitate smooth convergence and to eliminate negative frequencies, the opt=tight and integral=ultrafine keywords were compulsory for the M06-2X calculations. The B3LYP/6-311+G(d,p) frequencies were scaled by the recommended factor of 0.9887,[73] whereas the B3LYP-GD3BJ and M06-2X computed frequencies were used without scaling as excellent agreement was previously found between the frequencies predicted using these density functionals and the scaled B3LYP frequencies.[54]

Electrostatic potential (ESP) maps were computed for the B3LYP and M06-2X optimized geometries of the ground conformers of the [C_{n-2}mim:PF_6:$C_n$mim]$^+$ clusters. Favorable interaction sites of the [$C_n$mim]$^+$ cations and [PF_6]$^-$ anion, and how they are altered by the intrinsic binding interactions in the 2:1 cationic clusters are readily seen in these maps. All ESP maps were generated using a 6-311+G(2d,2p) basis set and are displayed at an isosurface of 0.01 a.u. of the total SCF electron density. The Mülliken charges on the hydrogen atoms of the [$C_n$mim]$^+$ cations and the fluorine atoms of the [PF_6]$^-$ anion are labeled. The most electronegative regions are shown in red, while the most electropositive regions are shown in blue.

Noncovalent interactions that stabilize the B3LYP and M06-2X ground conformers of the [C_{n-2}mim:PF_6:$C_n$mim]$^+$ clusters were calculated using the NCIPLOT method previously described by Yang and coworkers.[74,75] The NCIPLOT procedure reveals peaks in the reduced

View Article Online
DOI: 10.1039/D1CP02928B

electron density gradient that occur at low densities. The sign and magnitude of the product of the second density Hessian eigenvalue and the density distinguishes between attractive and repulsive interactions, and describes the strength of interactions, respectively. The NCI maps were rendered and visualized using Visual Molecular Dynamics (VMD) software,[76] and are shown at an isosurface of 0.20 a.u. of the reduced electron density gradient isosurfaces determined using the 6-311+G(2d,2p) basis set. Strong attractive interactions appear blue, e.g., hydrogen-bonding interactions; weak attractive interactions appear green, e.g., London dispersion interactions; whereas strong repulsive forces such as steric interactions appear red.

Thermochemical Analysis. The intensities of the precursor $[C_{n-2}mim:PF_6:C_nmim]^+$ cluster and CID fragment ions were measured as a function of collision energy and pressure of the neutral collision gas, Xe. The Beer's law relationship, $I = I_0 e^{-\sigma_{tot}\rho l}$, was used to convert the measured ion intensities to energy-dependent CID cross sections. Here I is the measured intensity of the precursor ion, I_0 is the total ion intensity (i.e., the sum of the precursor and CID product ion intensities), σ_{tot} is the total CID cross section, ρ is the collision gas density (P_{xe}/k_BT) where P_{xe} and T are the pressure and temperature of Xe and k_B is Boltzmann's constant, and l is the effective interaction path length (8.3 cm). The dc offset applied to the 8P is scanned to vary the collision energy, which also enables determination of the zero and width of the ion kinetic energy distribution.[77] The ion kinetic energy distributions of the $[C_{n-2}mim:PF_6:C_nmim]^+$ clusters measured here are well described by Gaussian distributions with a full width at half maximum (fwhm) of ~ 0.3–0.4 eV in the laboratory frame. Energies in the laboratory frame are converted to energies in the center-of-mass frame using the relationship, $E_{cm} = mE_{lab}/(m+M)$, where m is the mass of the neutral collision gas Xe and M is the mass of the precursor $[C_{n-2}mim:PF_6:C_nmim]^+$ cluster ion. Pressure-dependent studies are performed because multiple collisions of even a very small population of the precursor ion beam may impact the shape of CID cross sections, particularly in the threshold region, and shift the apparent threshold to lower collision energies.[60] The CID cross sections were measured at nominal Xe pressures of 0.20,

View Article Online
DOI: 10.1039/D1CP02928B

0.10, and 0.05 mTorr, and pressure extrapolated to zero pressure to analytically remove the effects of secondary collisions.

The fitting procedures employed for the thermochemical analysis of CID cross sections have evolved as new insights into energy transfer and dynamics of CID processes as well as modeling of the rates of unimolecular decomposition have been garnered, and have been discussed in detail previously.[57,78,79] Thresholds are determined via fitting using an empirical threshold law based on a modified line-of-centers collision theory model of the form,

$$\sigma(E) = \sigma_0 \sum_i g_i (E + E_i - E_0)^n / E \qquad \textbf{(2)}$$

where σ_0 is an energy-independent scaling factor, E is the relative translational energy of the $[C_{n-2}mim:PF_6:C_nmim]^+$ IL cluster and Xe reactants, E_0 is the threshold for reaction of the ground electronic and ro-vibrational state, and n is an adjustable parameter that describes the efficiency of kinetic to internal energy transfer.[57,78,79] The summation is over the ro-vibrational states of the $[C_{n-2}mim:PF6:C_nmim]^+$ cluster i, where E_i is the excitation energy of each state and g_i is the population of that state, ($\Sigma g_i = 1$). The density of ro-vibrational states is determined using the Beyer-Swinehart algorithm.[80] The relative populations g_i are calculated assuming a Maxwell-Boltzmann distribution of the precursor $[C_{n-2}mim:PF_6:C_nmim]^+$ cluster at 298 K.

Equation 2 provides robust modeling of CID cross sections only in cases where the rate of dissociation is very rapid such that the activated precursor ions dissociate before they enter the quadrupole mass filter. However, this is typically the case only for systems that are much smaller and less strongly bound than the $[C_{n-2}mim:PF_6:C_nmim]^+$ clusters examined here. To properly account for dissociation not occurring on the timescale of the experiments (~ 100 μs in our GIBMS instrument), the empirical threshold law of **eqn (2)** is modified to incorporate lifetime effects using Rice-Ramsperger-Kassel-Marcus (RRKM) theory as described by **eqn (3)**, and detailed previously.[78,81]

$$\sigma(E) = \left(\frac{n\sigma_0}{E}\right) \sum g_i \int_0^{E + E_i - E_0} [1 - e^{-k(E^*)\tau}](\Delta E)^{n-1} d(\Delta E) \qquad \textbf{(3)}$$

View Article Online
DOI: 10.1039/D1CP02928B

The integration of **eqn (3)** is over the dissociation probability, $k(E^*)$ is the unimolecular dissociation rate constant, and $E^* = E + E_i + \Delta E$, is the internal energy of the energized $[C_{n-2}mim{:}PF_6{:}C_nmim]^+$ cluster after it has collided with a Xe atom.

Equation 3 provides robust modeling of CID cross sections that exhibit a single primary dissociation pathway. However, if dissociation occurs via two or more competing pathways of similar energy, then the apparent threshold for the less favorable pathway is shifted to higher energy, a "competitive shift". To properly account for the effects of such competitive dissociation and enable extraction of accurate energetics, the empirical threshold law of **eqn (3)** is modified to enable simultaneous analysis of competitive dissociation pathways as described previously, **eqn (4)**.[78,79]

$$\sigma(E) = \left(\frac{n\sigma_{0,j}}{E}\right) \sum g_i \int_0^{E + E_i - E_{0,j}} \frac{k_j(E^*)}{k_{tot}(E^*)} [1 - e^{-k_{tot}(E^*)\tau}] (\Delta E)^{n-1} d(\Delta E) \qquad \textbf{(4)}$$

This modified form of the empirical threshold law incorporates competition between CID pathways where the subscript j designates the individual CID pathways. Competition is described by the ratio of the unimolecular dissociation rate constant for an individual CID pathway, $k_j(E^*)$, vs. the total unimolecular dissociation rate constant, $k_{tot}(E^*)=\Sigma k_j(E^*)$. Based on this model, the $\sigma_{0,j}$ values that describe the competitive dissociation behavior should in principle be the same for both dissociation pathways. However, we have previously found that CID cross sections cannot always be accurately reproduced unless the $\sigma_{0,j}$ values are not constrained to be equal to one another.[79,82-87] Thus, data was first analyzed using a single σ_0 value for the competitive dissociation channels. In cases where the data could not be accurately reproduced in this fashion, the $\sigma_{0,j}$ values were allowed to independently vary to enable reproduction of the experimental cross sections with enhanced fidelity.

The zero-pressure-extrapolated CID cross sections are modeled using **eqn (2)**, **eqn (3)**, and **eqn (4)**. Threshold energies extracted using **eqn (4)** provide accurate energetics for these systems, whereas values extracted from analyses using **eqn (3)** do not correct for competitive

View Article Online
DOI: 10.1039/D1CP02928B

effects and those using **eqn (2)** do not correct for lifetime or competitive effects. Comparisons of values extracted from these various analyses enable the lifetime and competitive effects to be independently assessed, and kinetic and competitive shifts in the CID cross sections to be quantitatively determined.

The errors in the threshold energies determined include variances from analyses of multiple datasets, uncertainties in the vibrational frequencies predicted by theory and their resultant impacts on the estimation of internal energy and RRKM lifetimes for dissociation, and the error in the absolute energy scale. Uncertainties introduced in the threshold determinations attributed to errors in the vibrational frequencies were estimated by scaling the predicted frequencies up and down by 10%, and by increasing and decreasing the time assumed available for dissociation by a factor of two. The absolute energy scale has an uncertainty of ±0.05 eV in the laboratory frame, which is limited by the voltage output of the 8P dc power supply. When converted to the center-of-mass frame this translates to an uncertainty of ~ ±0.02 eV (cm) for the $[C_{n-2}mim:PF_6:C_nmim]^+$ clusters examined here.[77] Uncertainties in the absolute cross section magnitudes have been previously estimated to be ~ ±20%; uncertainties in the relative cross section magnitudes are smaller due to cancellation of errors, and have been estimated to be ~ ±5%.[77]

RESULTS

Cross Sections for Collision-Induced Dissociation. Energy-dependent CID cross sections were measured for the interaction of three $[C_{n-2}mim:PF_6:C_nmim]^+$ clusters with Xe, where n = 4, 6 and 8. Data for all three clusters are displayed in the comparison of **Figure 2**. The dominant fragmentation pathways observed for all three clusters involve competitive loss of a neutral ion pair and detection of the complementary cation as described by **reactions (5)** and **(6)**.

$$[C_{n-2}mim:PF_6:C_nmim]^+ + Xe \rightarrow [C_nmim]^+ + (C_{n-2}mim:PF_6) + Xe \quad \textbf{(5)}$$

$$\rightarrow [C_{n-2}mim]^+ + (C_nmim:PF_6) + Xe \quad \textbf{(6)}$$

View Article Online
DOI: 10.1039/D1CP02928B

For all three clusters, the $[C_n\text{mim}]^+$ product cross section, **reaction (5)** exhibits a slightly lower apparent threshold and a larger magnitude over the entire range of collision energies examined than the $[C_{n-2}\text{mim}]^+$ product cross section, **reaction (6)**. The competitive CID data for each of the three clusters immediately establish the relative order of intrinsic binding of the $[C_n\text{mim}]^+$ cations to $[PF_6]^-$ as $[C_n\text{mim}]^+ < [C_{n-2}\text{mim}]^+$ because internal energy and lifetime effects influence both dissociation pathways in an equivalent manner. Combined these data indicate a relative order of binding to $[PF_6]^-$ of: $[C_8\text{mim}]^+ < [C_6\text{mim}]^+ < [C_4\text{mim}]^+ < [C_2\text{mim}]^+$. However, to quantitatively determine the absolute binding affinities of these $[C_n\text{mim}]^+$ cations for $[PF_6]^-$, thermochemical analyses that include the effects of the kinetic and internal energy distributions of the $[C_{n-2}\text{mim}{:}PF_6{:}C_n\text{mim}]^+$ and Xe reactants and the lifetime for dissociation including the effects of competition are necessary. Sequential dissociation of the $[C_n\text{mim}]^+$ and $[C_{n-2}\text{mim}]^+$ cations is observed at collision energies in excess of 4.5 eV. The 3-methylimidazolium cation, $[C_4H_7N_2]^+$, formed via neutral loss of the 1-alkyl substituent is the dominant sequential CID product observed. Additional $[C_nH_{2n+1}]^+$ cation series that arise from cleavage along and charge retention by the 1-alkyl substituent are also observed. The sequential dissociation pathways observed here for the $[C_n\text{mim}]^+$ cations parallel those observed previously;[54-56] results are summarized in **Table S1** (ESI†).

As can be seen in **Figure 2**, the energy-dependent CID behavior observed for all three $[C_{n-2}\text{mim}{:}PF_6{:}C_n\text{mim}]^+$ clusters is quite parallel. The cross section shapes are highly similar, while the cross section magnitudes and apparent onsets for dissociation do exhibit minor systematic variations. As both the absolute binding energies and trends in the binding of these clusters are of great interest, the total CID cross sections and the $[C_n\text{mim}]^+$ and $[C_{n-2}\text{mim}]^+$ primary product cross sections are compared in greater detail in **Figure 3**. As can be seen in the expanded overlays shown in the figure, the apparent thresholds for the total CID cross sections as well as the $[C_n\text{mim}]^+$ and $[C_{n-2}\text{mim}]^+$ primary product cross sections are very similar, but do exhibit a small systematic increase with the size of the cluster: 2:4 < 4:6 < 6:8 where n–2:n denotes the $[C_{n-2}\text{mim}{:}PF_6{:}C_n\text{mim}]^+$ cluster. The trend in the apparent thresholds suggest that the

View Article Online
DOI: 10.1039/D1CP02928B

binding is the weakest for the cluster involving the smallest cations and increases slightly with increasing size of the cations or lengths of the 1-alkyl chains. However, extracting meaningful trends from the apparent CID thresholds even for such highly parallel systems can be problematic, especially for systems that exhibit very minor differences in their energy dependences. This is particularly true for the $[C_{n-2}mim:PF_6:C_nmim]^+$ clusters examined here as the effects of the size of the cations on the internal energies and lifetimes for dissociation should shift the observed CID cross sections in opposite directions, and the magnitudes of these effects may differ. Comparison of the apparent thresholds for the $[C_nmim]^+$ and $[C_{n-2}mim]^+$ primary product cross sections from each $[C_{n-2}mim:PF_6:C_nmim]^+$ cluster makes it clear that binding to the larger cation is weaker. Therefore, the trends in the apparent thresholds indicate that lifetime effects impact the apparent thresholds to a greater extent than the internal energies for this cluster series.

Theoretical Results. Stable structures and energetics of the $[C_{n-2}mim:PF_6:C_nmim]^+$ clusters were calculated as described in the Theoretical calculations section. The structures and stabilities of the $[C_nmim]^+$ and $[PF_6]^-$ ions and $(C_nmim:PF_6)$ ion pairs are taken from our initial studies.[54,55] Details of the B3LYP, B3LYP-GD3BJ, and M06-2X geometry-optimized structures of the ground conformers of the $[C_nmim]^+$ cations, $[PF_6]^-$ anion, $(C_nmim:PF_6)$ ion pairs, and $[C_{n-2}mim:PF_6:C_nmim]^+$ clusters are given in **Tables S2-S5** (ESI†). The nomenclature used to differentiate the stable conformations of the $[C_nmim]^+$ cations, $(C_nmim:PF_6)$ ion pairs, and the $[C_{n-2}mim:PF_6:C_nmim]^+$ clusters is described in detail in **Figure S1** (ESI†).

$[C_nmim]^+$. Geometric parameters of the B3LYP, B3LYP-GD3BJ, and M06-2X geometry-optimized structures of the ground conformers of the $[C_nmim]^+$ cations are summarized in **Table S2** (ESI†). To visualize noncovalent interactions within these cations, NCI plots have been superimposed on the B3LYP ground conformers of the $[C_nmim]^+$ cations in **Figure 4**; a similar comparison of the B3LYP and M06-2X structures is provided in **Figure S2** (ESI†). The $[C_nmim]^+$ cations are simply denoted by a series of dihedral angles (a1...an that describe the conformation of the 1-alkyl substituent) enclosed in square brackets and

View Article Online
DOI: 10.1039/D1CP02928B

superscripted with a plus sign to indicate that they are cations, $[a1...an]^+$. See **Figure S1** (ESI†) for definitions of the 1-alkyl dihedral angles (an) and their cis, gauche(+), trans, and gauche(-) designations.

In the B3LYP ground conformers of the $[C_n mim]^+$ cations, the 1-alkyl substituents adopt anti-staggered orientations to minimize steric repulsion and are described as $[g_-]^+$, $[g_-t_2]^+$, $[g_-t_4]^+$, and $[g_-t_6]^+$ for n = 2, 4, 6, and 8, respectively. Of note, the g_+ and g_- designations for the a1 dihedral angle differentiate enantiomeric structures such that there are also energetically equivalent B3LYP ground conformations of the $[C_n mim]^+$ cations described as $[g_+]^+$, $[g_+t_2]^+$, $[g_+t_4]^+$, and $[g_+t_6]^+$, respectively. The NCI surfaces visible in the B3LYP optimized structures show no intramolecular stabilizing interactions. The ground conformers of the $[C_n mim]^+$ cations determined via M06-2X and B3LYP-GD3BJ optimization are similar to those determined by B3LYP except that twisting of the 1-alkyl chain to enable noncovalent interactions with the π cloud of the imidazolium ring is observed in these conformations, see **Figure S2** (ESI†). A weak interaction between the C2′ hydrogen atom and the C5 carbon atom of the imidazolium ring is evident in the NCI maps for all four cations. For the three largest cations, the longer 1-alkyl chain enables a much stronger noncovalent interaction between the C3′ hydrogen atom and the π cloud of the imidazolium ring. The excess charge is delocalized along the entire surface of the $[C_n mim]^+$ cation such that all of the hydrogen atoms provide favorable sites for accepting electron density from the anion. The charge of the imidazolium ring hydrogen atoms exceeds that of the 1-alkyl chain hydrogen atoms, with the greatest Mülliken charge on the C2 hydrogen atom. Additional details regarding the ground and other stable low-energy conformations of the $[C_n mim]^+$ cations computed can be found in our initial study of the $[2C_n mim{:}BF_4]^+$ clusters.[55]

$[PF_6]^-$ Anion. Geometric parameters of the B3LYP, B3LYP-GD3BJ, and M06-2X geometry optimized structures of the $[PF_6]^-$ anion are summarized in **Table S3** (ESI†). Noncovalent interactions are revealed using NCI plots superimposed on the B3LYP optimized structures of the $[PF_6]^-$ anion in **Figure 4**. Only a single conformer was found for $[PF_6]^-$ exhibiting an ideal octahedral geometry (with ∠FPF bond angles of 90.0º and P–F bond lengths

View Article Online
DOI: 10.1039/D1CP02928B

of 1.646 Å). The P–F bond lengths in the M06-2X structure are slightly shorter than those computed by B3LYP and B3LYP-GD3BJ. The F atom lone pairs of electrons provide favorable sites for donation of electron density to the $[C_n\text{mim}]^+$ cations.

($C_n$mim:PF_6). Geometric parameters of the B3LYP, B3LYP-GD3BJ, and M06-2X geometry-optimized structures of the ground conformers of the ($C_n$mim:PF_6) ion pairs are summarized in **Table S4**. NCI plots superimposed on the B3LYP ground conformers of the ($C_n$mim:PF_6) ion pairs are shown in **Figure 5** to visualize noncovalent interactions within these ion pairs; a similar comparison of the B3LYP and M06-2X structures is provided in **Figure S3** (ESI†). The intrinsic binding interactions of the ground conformers of the ($C_n$mim:PF_6) ion pairs are conserved across the cation series and the various levels of theory examined. Other less favorable modes of binding were also found among the stable conformers. Therefore, the ($C_n$mim:PF_6) ion pairs are denoted by the mode of binding and the dihedral angles that describe the conformation of the 1-alkyl chain enclosed in parentheses, the absence of charge indicates that these conformers are neutral ion pairs, (**b1BS**;a1...an). See **Figure S1** (ESI†) for the various binding site designations, which provide details of the location and orientation of the binding interactions. The B3LYP and M06-2X ground conformers of the ($C_n$mim:PF_6) ion pairs all exhibit front-side binding (**F**), but several favorable orientations as described by the **b1** dihedral angle are found including $\mathbf{g}_+$, $\mathbf{g}_-$, and **c**. The 1-alkyl substituents adopt anti-staggered orientations in which the 1-alkyl chain partially folds around the anion to enhance stabilization.

The B3LYP ground conformers are described as (**g**$_+$**F**;g$_-$), (**g**$_+$**F**;g$_-$t$_2$), (**g**$_-$**F**;g$_-$t$_4$), and (**g**$_-$**F**;g$_-$t$_6$). Highly parallel to the B3LYP structures, the M06-2X ground conformers are described as (**g**$_-$**F**;g$_-$), (**g**$_-$**F**;g$_-$t$_2$), (**g**$_-$**F**;g$_-$t$_4$), and (**g**$_-$**F**;g$_-$t$_6$). Notably, the NCI surfaces of the B3LYP structures are less extensive than those determined via M06-2X, see **Figure S3** (ESI†). The cation-anion distance does not vary appreciably with the cation across the ($C_n$mim:PF_6) ion pair series, but does depend on the theoretical model employed with B3LYP finding a larger separation than B3LYP-GD3BJ and M06-2X. Additional structural and energetic information for the ground and other stable low-energy conformations of the ($C_n$mim:PF_6) ion pairs computed

View Article Online
DOI: 10.1039/D1CP02928B

can be found in our initial study of the $[2C_n\text{mim:PF}_6]^+$ clusters.[54] The structures predicted for the ($C_n$mim:PF_6) ion pairs are consistent with those previously reported for the ($C_n$mim:PF_6).[43,46-49] Structures of the ($C_n$mim:PF_6) ion pairs were reported in a computational study by Kamalakann et al. as (**g**$_+$**F**;g$_+$), (**g**$_+$**F**;g$_+$t$_2$), (**g**$_+$**F**;g$_+$t$_4$), and (**g**$_+$**F**;g$_+$t$_5$g$_+$) from the PBE+D3/6-311++G** level of theory.[48] The key binding interactions are conserved in all studies, whereas slight differences in the alkyl chain orientation in the computed ground conformers are likely associated with the use of different basis sets and the high degree of conformational flexibility available to these systems.

$[C_{n-2}$mim:PF_6:$C_n$mim$]^+$. Geometric parameters of the B3LYP, B3LYP-GD3BJ, and M06-2X geometry-optimized structures of the ground conformers of the $[C_{n-2}\text{mim:PF}_6\text{:}C_n\text{mim}]^+$ clusters are summarized in **Table S5** (ESI†). Noncovalent interactions within these clusters are again visualized with NCI plots superimposed on the B3LYP ground conformers in **Figure 6**, a similar comparison of the B3LYP and M06-2X ground conformers is included in **Figure S4** (ESI†). The $[C_{n-2}\text{mim:PF}_6\text{:}C_n\text{mim}]^+$ clusters are denoted by the modes of binding and the dihedral angles that describe the conformations of the 1-alkyl substituents enclosed in square brackets and superscripted with a plus sign to indicate that they are cations, [a1...an-2:**b2BS1**(n-2)**BS2**(n):a1...an]$^+$. To facilitate recognition, the 1-alkyl orientation of the $[C_{n-2}\text{mim}]^+$ cation and its binding mode is given first. See **Figure S1** (ESI†) for the various binding site designations, which provide details of the locations and orientations of the binding interactions as well as the relative orientations of the 1-alkyl substituents.

The B3LYP ground conformers are described as [g$_-$;**g_cFcF**;g$_-$t$_2$]$^+$, [g$_-$t$_2$;**g_cFcF**;g$_+$t$_4$]$^+$, and [g$_-$t$_4$;**g_cFcF**;g$_-$t$_6$]$^+$, whereas the M06-2X ground conformers are described as [g$_-$;**g_g$_+$Fg_F**;g$_-$t$_2$]$^+$, [g$_+$t$_2$;**g$_+$g$_+$Fg$_+$F**;g$_-$t$_4$]$^+$, and [g$_+$t$_4$;**g_g_Fg$_+$F**;g$_-$t$_6$]$^+$. Additional structural and energetic information for the ground and other stable low-energy conformations of the $[C_{n-2}\text{mim:PF}_6\text{:}C_n\text{mim}]^+$ clusters computed can be found in the comparisons of **Figures S5-S7** (ESI†), which include their B3LYP, B3LYP-GD3BJ, and M06-2X relative Gibbs energies. ESP maps of the ground conformers of the $[C_{n-2}\text{mim:PF}_6\text{:}C_n\text{mim}]^+$ clusters determined at the B3LYP

View Article Online
DOI: 10.1039/D1CP02928B

and M06-2X levels are compared in **Figure S8**. The stable low-energy $[C_{n-2}mim:PF_6:C_nmim]^+$ structures exhibit a preference for front side binding regardless of the theoretical model employed. Front binding favors noncovalent interactions between the C1′, C2, and C1″ hydrogen atoms of each of the cations and two of the F atoms of the $[PF_6]^-$ anion, with additional stabilization gained through an anion-π interaction between a third F atom and the π-cloud of each of the imidazolium rings, parallel to that observed in the $(C_nmim:PF_6)$ ion pairs. The 1-alkyl chains again take on anti-staggered geometries to minimize steric strain as favored by the $[C_nmim]^+$ cations.

Theoretical estimates for the BDEs of the $[C_{n-2}mim:PF_6:C_nmim]^+$ and $[2C_nmim:PF_6]^+$ clusters are predicted based on the computed ground conformers of these clusters and their $[C_nmim]^+$ cations and $(C_nmim:PF_6)$ ion pairs. As described earlier, the clusters dissociate via loss of a neutral ion pair; a single primary CID pathway is observed for the $[2C_nmim:PF_6]^+$ clusters, **reaction (1)**, whereas two primary CID pathways occur in competition for the mixed clusters **reactions (5)** and **(6)**. Theoretical estimates for the IPEs and ΔIPEs of the $(C_nmim:PF_6)$ ion pairs are also predicted based on the computed ground conformers of these ion pairs and the $[C_nmim]^+$ cations and the $[PF_6]^-$ anion.

Threshold Analysis of CID Cross Sections. The threshold regions of the zero-pressure extrapolated cross sections for the primary CID pathways, **reactions (5)** and **(6)**, observed for three $[C_{n-2}mim:PF_6:C_nmim]^+$ clusters were simultaneously modeled using the empirical threshold law of **eqn (4)** as described in the **Thermochemical Analysis** section. These simple noncovalent bond cleavage reactions were modeled using a loose phase space limit transition state (PSL TS) model.[78,79] Previous work has established the PSL TS model as providing the most accurate determination of threshold energies for CID reactions of noncovalently bound complexes.[88-95] Representative analyses for all three clusters are compared in **Figure 7**. As can be seen in the figure, the PSL TS model reproduces the primary CID product cross sections for all three $[C_{n-2}mim:PF_6:C_nmim]^+$ clusters with high fidelity over energy ranges exceeding 2.5 eV and cross sections magnitudes of at least 100. Results of these analyses are summarized in **Table**

View Article Online
DOI: 10.1039/D1CP02928B

1. The primary CID product cross sections were also independently modeled using the empirical threshold law of **eqn (3)**; results of these analyses are summarized in **Table S6** (ESI†). Comparison of results of analyses using **eqn (3)** and **eqn (4)** enable competitive shifts in the CID product cross sections to be quantitatively assessed. The primary CID product cross sections were also independently modeled using **eqn (2)** in two ways, in the first the *n* values for both pathways are fixed at the value determined from analysis with **eqn (4)**, and in the second, the *n* values are set at the values determined from **eqn (3)**. Comparison of results of analyses for **eqn (2)** and **eqn (4)** and likewise comparisons of analyses using **eqn (2)** and **eqn (3)** enable kinetic shifts to be quantitatively assessed. Results of analyses using **eqn (2)** are also summarized in **Table 1** and **Table S6** (ESI†). The molecular parameters employed for all thermochemical analysis are taken from the B3LYP optimized structures of the ground conformers of the precursor $[C_{n-2}mim:PF_6:C_nmim]^+$ cluster and its CID products, which are summarized in **Tables S7** and **S8** (ESI†).

Kinetic Shifts. The differences between the threshold values determined including lifetime effects, **eqn (4)** and **eqn (3)**, E_0(PSL), and those excluding lifetime effects, **eqn (2)**, E_0, provide quantitative assessment of the kinetic shifts in the experimental data and are also given in **Table 1** and **Table S6** (ESI†). The kinetic shifts are appreciable and vary with the size of the cluster. The kinetic shifts are smallest for the $[C_2mim:PF_6:C_4mim]^+$ cluster with values of 0.91 and 0.84 eV for **reactions (5)** and **(6)** when modeled competitively, and 0.90 and 0.88 eV when modeled independently. The kinetic shifts are somewhat larger for the $[C_4mim:PF_6:C_6mim]^+$ cluster with values of 1.15 and 1.12 eV when modeled competitively, and 1.16 and 1.17 eV when modeled independently. The kinetic shifts are largest for the $[C_6mim:PF_6:C_8mim]^+$ cluster with values of 1.47 and 1.38 eV when modeled competitively, and 1.57 and 1.55 eV when modeled independently. Competitive effects are seen in these analyses as the kinetic shifts of the $[C_{n-2}mim]^+$ product cross sections, **reaction (6)** is influenced by the mode of analysis (competitive vs. independent) to a greater extent than the $[C_nmim]^+$ product cross sections, for the lowest-energy pathway, **reaction (5)**. Trends in the kinetic shifts are easily rationalized based

View Article Online
DOI: 10.1039/D1CP02928B

on the number of vibrational modes present in these clusters, which increase from 147 to 183 to 219, respectively. The very minor differences in the kinetic shifts determined from analyses that include and exclude the effects of competition indicate that the energetics for both dissociation pathways are very similar, consistent with the thresholds determined.

Competitive Shifts. The differences between the threshold values, E_0(PSL), determined including and excluding competitive effects, **eqn (4)** and **eqn (3)**, provide quantitative assessment of the competitive shifts in the experimental data and are rather small for these systems. The threshold values for **reactions (5)** and **reactions (6)** generally increase by 0.01-0.02 eV and at most 0.05 eV when competition is included. These results are consistent with previous findings where errors resulting from "competitive shifts" were found to be small when thresholds differ by ~ 0.1 eV or less.[79]

The entropy of activation, $\Delta S^{\ddagger}$, is a measure of the looseness of the TS but also depends on the size and complexity of the system. The entropy of activation is determined as the entropy difference between the TS employed in the modeling of the data, a PSL TS for the noncovalently bound IL cluster examined here, and the reactants. The $\Delta S^{\ddagger}$(PSL) values at 1000 K determined for analyses using **eqn (4)** and **eqn (3)** are included in **Table 1** and **Table S6** (ESI†). The values span only a modest range and vary between 5 and 24 J mol^{-1} K^{-1} across these $[C_{n-2}mim:PF6:C_nmim]^+$ clusters. The values of $\Delta S^{\ddagger}$ are positive as expected for unimolecular dissociation reactions of noncovalently bound systems, and in particular for modeling using a loose PSL TS as employed here. These values compare favorably to $\Delta S^{\ddagger}$ values previously determined for CID of noncovalently bound complexes that have been previously measured in our laboratory.[88-94]

Conversion from 0 to 298 K. Although TCID measurements are typically performed at room temperature as for the systems examined here, the effects of experimental broadening are removed such that the values extracted from thermochemical analyses correspond to enthalpies of dissociation at 0 K. The 0 K enthalpies (or 0 K BDEs) are converted to 298 K enthalpies and free energies of binding to facilitate comparisons to values typically reported in the literature.

View Article Online
DOI: 10.1039/D1CP02928B

The enthalpy and entropy conversions are calculated using standard formulas based on harmonic oscillator and rigid rotor models and computed using the vibrational frequencies and rotational constants determined from the B3LYP optimized geometries, which are given in **Tables S7** and **S8** (ESI†). **Table 2** lists the 0 and 298 K enthalpy, free energy, and entropic corrections for all systems experimentally determined. Uncertainties in the enthalpic and entropic corrections are estimated by ±10% variation in the vibrational frequencies.

DISCUSSION

Comparison of Theory and Experiment: The ability of the B3LYP, B3LYP-GD3BJ and M06-2X theoretical approaches employed here to describe the intrinsic cation-anion interactions in the ($C_n$mim:PF_6) ion pairs and $[2C_n\text{mim:}PF_6]^+$ and $[C_{n-2}\text{mim:}PF_6\text{:}C_n\text{mim}]^+$ clusters is evaluated comprehensively. First comparisons between the measured and computed BDEs of the $[2C_n\text{mim:}PF_6]^+$ clusters previously determined are reviewed.[54] Comparisons are then made between the measured and computed BDEs of the $[C_{n-2}\text{mim:}PF_6\text{:}C_n\text{mim}]^+$ clusters determined here. Finally, the computed relative BDEs of the $[2C_n\text{mim:}PF_6]^+$ clusters and relative IPEs of the ($C_n$mim:PF_6) ion pairs are compared to those estimated from the measured relative BDEs of the $[C_{n-2}\text{mim:}PF_6\text{:}C_n\text{mim}]^+$ clusters determined here via competitive TCID measurements.

$[2C_n\text{mim:}PF_6]^+$ BDEs. Excellent agreement between the TCID measured BDEs of the $[2C_n\text{mim:}PF_6]^+$ clusters and those predicted by B3LYP was previously reported.[54] For B3LYP, a mean absolute deviation (MAD) between the computed and measured values of 1.6 ± 1.5 kJ/mol was found, which is smaller than the average experimental uncertainty (AEU) in the measured values, 5.3 ± 0.9 kJ/mol. The MAD determined for M06-2X, 6.7 ± 4.3 kJ/mol, is of similar magnitude to the AEU. Much poorer agreement with the measured values was found using B3LYP-GD3BJ with a MAD of 10.4 ± 6.6 kJ/mol. Overall these comparisons suggest that the B3LYP and M06-2X values are the most reliable, where B3LYP-GD3BJ overestimates the strength of binding in the $[2C_n\text{mim:}PF_6]^+$ clusters.

View Article Online
DOI: 10.1039/D1CP02928B

$[C_{n-2}mim:PF_6:C_nmim]^+$ BDEs. The TCID measured BDEs of the $[C_{n-2}mim:PF_6:C_nmim]^+$ clusters are compared to the B3LYP values in **Figure 8**. Comprehensive comparisons to all three levels of theory are provided in **Table 3** and shown in **Figure S9** (ESI†). The experimental values listed in the table and plotted in the figure(s) are determined from threshold analyses based on the B3LYP optimized geometries of the precursor $[C_{n-2}mim:PF_6:C_nmim]^+$ cluster and its primary dissociation products. As found for the $[2C_nmim:PF_6]^+$ clusters, B3LYP predicts BDEs that are in excellent agreement with the values determined from the TCID measurements. The MAD between the TCID measured BDEs and the B3LYP calculated values is 1.9 ± 1.8 kJ/mol, which again is smaller than the AEU in these values, 5.7 ± 1.0 kJ/mol. M06-2X also does a very good job with a MAD of 6.8 ± 1.6 kJ/mol. Consistent with previous findings, B3LYP-GD3BJ does not perform as well with a MAD that is more than twice as large, 14.9 ± 8.3 kJ/mol. These comparisons again suggest that the B3LYP values are the most reliable, and that M06-2X performs respectably. However, B3LYP-GD3BJ does not perform well and systematically overestimates the strength of binding by approximately three times the AEU in the BDEs indicating that the approach for incorporating dispersion in this model is over-predicting the effects.

$[C_{n-2}mim:PF_6:C_nmim]^+$ Relative BDEs. The TCID measured relative BDEs of the $[C_{n-2}mim:PF_6:C_nmim]^+$ clusters are compared to B3LYP computed values in **Figure 9**. Comparisons to all three levels of theory are provided in **Table 4** and shown in **Figure S10** (ESI†). The experimental values listed in the table and plotted in the figures are again those determined from threshold analyses based on the B3LYP optimized geometries of the precursor $[C_{n-2}mim:PF_6:C_nmim]^+$ cluster and its primary dissociation products. The theoretical values are computed in two different ways, first as the relative BDEs (ΔBDEs) of the $[C_{n-2}mim:PF_6:C_nmim]^+$ clusters and their dissociation products, **reactions (5)** and **(6)**, and also as the relative ion pairing energies (ΔIPEs) of the ($C_nmim:PF_6$) and ($C_{n-2}mim:PF_6$) ion pairs. The differences in the computed ΔBDEs vs. ΔIPEs is small regardless of theory, with B3LYP (0.7 to 0.9 kJ/mol), B3LYP-GD3BJ (0.6 to 1.6 kJ/mol), and M06-2X (0.2 to 2.0 kJ/mol). The MAD

View Article Online
DOI: 10.1039/D1CP02928B

between the TCID measured ΔBDEs and the B3LYP computed ΔBDEs is 1.9 ± 1.4 kJ/mol, and even smaller when compared to the B3LYP predicted ΔIPEs, 1.6 ± 1.2 kJ/mol. Similar performance is found by M06-2X, with MADs of 1.0 ± 1.3 kJ/mol and 1.5 ± 1.1 kJ/mol. Only slightly larger differences are observed for B3LYP-GD3BJ with MADs between the TCID measured ΔBDEs and the B3LYP-GD3BJ computed values of 2.2 ± 2.9 kJ/mol and 2.1 ± 1.5 kJ/mol. All three levels of theory find similar MADs between the measured ΔBDEs and the calculated ΔIPEs and the measured ΔBDEs and the calculated ΔBDEs. These comparisons suggest that all three levels of theory explored here are able to predict the relative energetics for these systems very well.

Ion Pairing Energies. Based on these findings, we report theoretical estimates for the absolute IPEs of the ($C_n$mim:PF_6) ion pairs, which are summarized in **Table 5**. For all three theoretical models, the computed IPEs are quite large and nearly three times as large at the BDEs measured and predicted for the $[2C_n\text{mim:PF}_6]^+$ and $[C_{n-2}\text{mim:PF}_6\text{:}C_n\text{mim}]^+$ clusters, and generally decrease with increasing size of the cation. The B3LYP predicted IPEs are the weakest ~ 314 kJ/mol, increase for B3LYP-GD3BJ to ~ 341 kJ/mol, and increase further to ~ 346 kJ/mol for M06-2X. The smallest (C_2mim:PF_6) ion pair is predicted to have the greatest IPE for all levels of theory explored. The larger ion pairs ($C_n$mim:PF_6), where n = 4, 6, and 8 have predicted IPEs that are approximately equal for each level of theory. These results are in good agreement with the previously calculated IPEs of ~333 kJ/mol at the PBE/6-311++G(d,p) level of theory increasing to ~352 kJ/mol when D3 dispersion is included.[48]

Evaluated $[2C_n\text{mim:PF}_6]^+$ BDEs. As discussed above, the variation in the BDEs of the $[2C_n\text{mim:PF}_6]^+$ clusters determined from independent TCID experiments is small, and similar in magnitude to the AEU in these determinations.[54] Thus, the absolute order of the intrinsic binding interactions as a function of the cation cannot be established solely from these measurements. However, the competitive dissociation behavior of the $[C_{n-2}\text{mim:PF}_6\text{:}C_n\text{mim}]^+$ clusters examined here definitively establish the relative order of binding of the $[2C_n\text{mim:PF}_6]^+$ clusters as a function of the cation as: $[C_8\text{mim}]^+ < [C_6\text{mim}]^+ < [C_4\text{mim}]^+ < [C_2\text{mim}]^+$. Further, the relative

View Article Online
DOI: 10.1039/D1CP02928B

BDEs determined here provide additional constraints on the absolute energetics of binding in these clusters, and with reduced uncertainties. By combining the absolute BDEs of the $[2C_n\text{mim:PF}_6]^+$ clusters with the relative BDEs of the $[C_{n-2}\text{mim:PF6:C}_n\text{mim}]^+$ clusters determined here and subjecting the results to linear regression/maximum likelihood analysis using OriginPro 8.6.0 (OriginLab Corporation, Northampton, MA, USA), improved estimates of the BDEs of the $[2C_n\text{mim:PF}_6]^+$ clusters are determined. The results of these combined analyses are summarized in **Table 6** and shown in **Figure 10**. The absolute BDEs of the $[2C_n\text{mim:PF}_6]^+$ clusters previously determined from independent TCID measurements are plotted in the top panel of **Figure 10** (open symbols). The relative BDEs of the $[2C_n\text{mim:PF}_6]^+$ clusters, which are equated with the relative BDEs of the $[C_{n-2}\text{mim:PF}_6\text{:C}_n\text{mim}]^+$ clusters determined from competitive TCID measurements (as validated above) are plotted in the bottom panel of **Figure 10**. Combined, this thermochemistry provides an over-determined system of equations that was solved to extract BDEs of the $[2C_n\text{mim:PF}_6]^+$ clusters with improved accuracy and precision as shown in the top panel of **Figure 10** (closed symbols). While the BDEs determined directly from the $[2C_n\text{mim:PF}_6]^+$ clusters do not differ significantly from the BDEs determined from the over-determined system of equations, the increased precision greatly reduces the magnitude of the uncertainty of the determinations. The span of these BDEs now exhibit very little overlap due to the increased precision, firmly establishing the relative order of binding as $[C_8\text{mim}]^+ < [C_6\text{mim}]^+ < [C_4\text{mim}]^+ < [C_2\text{mim}]^+$. These results are consistent with the previously published ESI-MS/MS results using collisional activation to examine the dissociation behavior of IL clusters and to establish cation-anion interaction scales for ILs.[25-32] These works report relative interaction scales for a variety of $[C_n\text{mim}]^+$ cations with multiple anions including $[\text{Br}]^-$, $[\text{Cl}]^-$, $[\text{BF}_4]^-$, $[\text{Tf}_2\text{N}]^-$ and strongest binding interactions with the smaller $[C_n\text{mim}]^+$ cations. Our work expands on theirs by providing absolute binding affinities or BDEs of the $[2C_n\text{mim:PF}_6]^+$ and $[C_{n-2}\text{mim:PF}_6\text{:C}_n\text{mim}]^+$ IL clusters under investigation.

The BDEs of the $[2C_n\text{mim:PF}_6]^+$ clusters originally measured as well as those derived from the regression analysis are compared with the B3LYP predicted BDEs in **Figure 11**. A

View Article Online
DOI: 10.1039/D1CP02928B

similar comparison to all three levels of theory is provided in **Figure S11** (ESI†). The agreement between the measured BDEs derived from the regression analysis and the B3LYP calculated BDEs is again excellent with a MAD of 1.8 ± 1.2 kJ/mol. The MAD for M06-2X, 6.8 ± 2.8 kJ/mol, is similar to the AEU, whereas that for B3LYP-GD3BJ, exceeds the AEU by a factor of two. Notably, the agreement between theory and experiment is not significantly altered whether the directly measured or evaluated BDEs are used. Overall, these results suggest that all three levels of theory are able to provide a reasonable description of the binding in these systems with B3LYP providing the best performance, M06-2X providing very good performance, and B3LYP-GD3BJ providing somewhat less reliable results.

CID Behavior of $[2C_n\text{mim:}PF_6]^+$ vs. $[2C_n\text{mim:}BF_4]^+$ Clusters. The energy-dependent CID behavior of the $[2C_n\text{mim:}PF_6]^+$ clusters is highly parallel to that of the analogous $[2C_n\text{mim:}BF_4]^+$ clusters.[55,56] The dominant fragmentation pathway for all clusters involves the loss of an intact ($C_n\text{mim:}PF_6$) or ($C_n\text{mim:}BF_4$) ion pair from the IL cluster. The BDEs determined via thermochemical analysis exhibit only very minor variation across both the cation and anion series. The impact of the anion is observed in the strength of cation binding compared in **Figure 12**. Cation binding in the $[2C_n\text{mim:}PF_6]^+$ clusters is ~6.3% weaker than that in the $[2C_n\text{mim:}BF_4]^+$ clusters. The weaker binding of $[C_n\text{mim}]^+$ to ($C_n\text{mim:}PF_6$) than ($C_n\text{mim:}BF_4$) is attributed to the larger size and thus increased diffusivity of the $[PF_6]^-$ anion. The impact of $[C_n\text{mim}]^+$ cation on the strength of cation binding is parallel for both the $[2C_n\text{mim:}PF_6]^+$ and $[2C_n\text{mim:}BF_4]^+$ clusters. For both IL cluster types binding is the strongest for the smallest cations. The competitive dissociation experiments and evaluated BDEs of the $[2C_n\text{mim:}PF_6]^+$ and $[2C_n\text{mim:}BF_4]^+$ clusters conclusively reveal the absolute order of binding among these clusters to follow the order: $[C_8\text{mim}]^+ < [C_6\text{mim}]^+ < [C_4\text{mim}]^+ < [C_2\text{mim}]^+$. Parallel size and diffusivity effects are observed in the cation binding trends for both the $[2C_n\text{mim:}PF_6]^+$ and $[2C_n\text{mim:}BF_4]^+$ clusters; the strongest binding occurs for the smallest cations. These results indicate that the more charge dense cations and anions produce the strongest binding in the 1-alkyl-3-methylimidazolium IL clusters studied here with the $[PF_6]^-$ and $[BF_4]^-$ anions.

View Article Online
DOI: 10.1039/D1CP02928B

The similar strength of binding and reactivity observed in the $[2C_n\text{mim:}PF_6]^+$ and $[2C_n\text{mim:}BF_4]^+$ IL clusters is readily explained by the similar structures predicted using the density function theory methods employed here. The optimized structures predicted for the ($C_n\text{mim:}PF_6$) and ($C_n\text{mim:}BF_4$) ion pairs are very similar with similar NCIs. In all of the ion pairs, front binding of the imidazolium cation to the anion is preferred with binding occurring via noncovalent interactions between the C1′, C2, and C1″ hydrogen atoms of the $[C_n\text{mim}]^+$ cation and two of the F atoms of the anion, while a third F atom interacts with the π-cloud of the imidazolium ring. Likewise, the optimized structures predicted for the $[2C_n\text{mim:}PF_6]^+$ and $[2C_n\text{mim:}BF_4]^+$ clusters and their respective ion pairs are similar and stabilized by parallel NCIs, resulting in similar determined BDEs. Both clusters favor binding to the front of the imidazolium ring and the preference for the 1-alkyl substituent to adopt an elongated conformation resulting in $[g_+t_{n-2}]^+$ and $[g_-t_{n-2}]^+$ conformers (B3LYP). Cation binding in the $[2C_n\text{mim:}BF_4]^+$ clusters was predicted to be nearly planar in their front binding interactions with two fluorine atoms of $[BF_4]^-$. In contrast, cation binding in $[2C_n\text{mim:}PF_6]^+$ occurs with three fluorine atoms of $[PF_6]^-$, a binding motif consistent with that found in the ($C_n\text{mim:}PF_6$) and ($C_n\text{mim:}BF_4$) ion pairs. This difference in binding in the 2:1 clusters is clearly attributable to the availability of six fluorine donors in $[PF_6]^-$, whereas only four are available in $[BF_4]^-$. The high similarity of the predicted structures results in an ~6.3% decrease in the predicted strength of binding in the $[2C_n\text{mim:}PF_6]^+$ clusters vs. their $[2C_n\text{mim:}BF_4]^+$ cluster analogues.

CONCLUSIONS

Competitive TCID measurements and electronic structure calculations were performed to examine the energy-dependent dissociation behavior and determine the bond dissociation energies (BDEs) of three mixed $[C_{n-2}\text{mim:}PF_6\text{:}C_n\text{mim}]^+$ clusters, for n = 4, 6, and 8. The competitive dissociation behavior examined here, definitively establishes the relative order of binding among all three clusters as $[C_n\text{mim}]^+ < [C_{n-2}\text{mim}]^+$. In our previous study, four $[C_n\text{mim}]^+$ cations with 1-alkyl substituents of variable length were included in the work to examine the

View Article Online
DOI: 10.1039/D1CP02928B

structural and energetic effects of the size of the 1-alkyl substituent on the binding. The variation in the BDEs of the $[2C_n\text{mim:}PF_6]^+$ clusters was found to be similar to the AEU in the values[54] such that trends in the BDEs as a function of the cation were indiscernible, requiring the competitive TCID measurements reported here to definitively establish the relative strength of binding as accomplished. Further, enhanced accuracy and precision in these determinations is achieved via simultaneous thermochemical analyses of the competitive TCID data combined with the previous $[2C_n\text{mim:}PF_6]^+$ results[54] and maximum likelihood analyses. The evaluated BDEs of the $[2C_n\text{mim:}PF_6]^+$ clusters conclusively establish the absolute order of binding among these clusters as: $[C_8\text{mim}]^+ < [C_6\text{mim}]^+ < [C_4\text{mim}]^+ < [C_2\text{mim}]^+$. Overall, B3LYP and M06-2X are found to best describe the binding in $C_n\text{mim}–PF_6$ IL clusters, whereas somewhat poorer agreement is found for B3LYP-GD3BJ.

The very small variation in the energetics of binding as the cation is varied suggest that all four $C_n\text{mim}–PF_6$ ILs (n = 2, 4, 6 and 8) should provide similar efficiencies for electrospray propulsion. The results for the $C_n\text{mim}–PF_6$ ILs are highly parallel to those found previously for the $C_n\text{mim}–BF_4$ ILs (n = 2, 4, 6 and 8) with the strength of cation binding in the $C_n\text{mim}–PF_6$ clusters ~6.3% weaker than in the $C_n\text{mim}–BF_4$ clusters. However, packing effects may differ as a function of the cation such that differences in propulsion efficiency may be found when the electrospray thrusters are tuned to produce larger clusters with higher thrust/lower efficiency operation. Studies of larger clusters should elucidate packing effects and provide additional insight into the relative ability of these $C_n\text{mim}–PF_6$ and $C_n\text{mim}–BF_4$ ILs to serve as fuels for electrospray propulsion.

† Electronic supplementary information (ESI) available: Tables summarizing CID fragments of the $[C_{n-2}\text{mim:}PF_6\text{:}C_n\text{mim}]^+$ cluster ions; geometric parameters of the ground conformers of the $[C_n\text{mim}]^+$ cations, $[PF_6]^-$ anion, $(C_n\text{mim:}PF_6)$ ion pairs, and $[C_{n-2}\text{mim:}PF_6\text{:}C_n\text{mim}]^+$ clusters, fitting parameters of **eqn (3)** for threshold determinations in which the two primary CID product cross sections are fitted independently; molecular (vibrational and rotational) constants determined from B3LYP/6-311+G(d,p) optimized geometries of the $[C_{n-2}\text{mim:}PF_6\text{:}C_n\text{mim}]^+$ clusters, $(C_n\text{mim:}PF_6)$ ion pairs, and $[C_n\text{mim}]^+$ cations employed in the thermochemical analysis

View Article Online
DOI: 10.1039/D1CP02928B

of the experimental data. Figures describing the nomenclature used to differentiate various stable conformations of the $[C_{n-2}mim:PF_6:C_nmim]^+$ clusters, ($C_nmim:PF_6$) ion pairs, and $[C_nmim]^+$ cations; ground and select stable conformations of the $[C_{n-2}mim:PF_6:C_nmim]^+$ clusters found at the B3LYP/6-311+G(d,p), B3LYP-GD3BJ/6-311+G(d,p), and M06-2X/6-311+G(d,p) levels of theory along with their relative Gibbs free energies determined at the same levels of theory with a 6-311+G(2d,2p) basis set are provided; ESP maps of the B3LYP/6-311+G(2d,2p) ground conformers of the $[C_{n-2}mim:PF_6:C_nmim]^+$ clusters. Comparisons of B3LYP, B3LYP-GD3BJ, and M06-2X computed 0 K BDEs versus measured threshold dissociation energies of the $[C_{n-2}mim:PF_6:C_nmim]^+$ clusters, comparisons of B3LYP, B3LYP-GD3BJ, and M06-2X computed relative BDEs of the $[C_{n-2}mim:PF_6:C_nmim]^+$ clusters and relative IPEs of the ($C_nmim:PF_6$) ion pairs vs. experimentally determined 0 K ΔBDEs of the $[C_{n-2}mim:PF_6:C_nmim]^+$ clusters, comparisons of B3LYP, B3LYP-GD3BJ, and M06-2X computed vs. TCID 0 K BDEs of the $[2C_nmim:PF_6]^+$ clusters, all for n = 2, 4, 6, and 8 and in kJ/mol.

AUTHOR INFORMATION

Notes. The authors declare no competing financial interest.

ACKNOWLEDGMENTS

Financial support for this work was provided by the National Science Foundation, CHE-1709789. Computational resources were provided by Wayne State University C&IT. The authors acknowledge support from the Wayne State University Summer Dissertation Fellowship for HAR.

ORCID

Harrison A. Roy https://orcid.org/0000-0002-9128-5245

Mary T. Rodgers https://orcid.org/0000-0002-5614-0948

REFERENCES

1. D. R. MacFarlane, M. Kar and J. M. Pringle, *Fundamentals of Ionic Liquids: From Chemistry to Applications*, John Wiley & Sons, 2017.
2. H. Liu, Y. Liu and J. Li, *Phys. Chem. Chem. Phys.*, 2010, **12**, 1685-1697.
3. D. R. MacFarlane, M. Forsyth, P. C. Howlett, J. M. Pringle, J. Sun, G. Annat, W. Neil and E. I. Izgorodina, *Accts. Chem. Res.*, 2007, **40**, 1165-1173.
4. M. Watanabe, M. L. Thomas, S. Zhang, K. Ueno, T. Yasuda and K. Dokko, *Chem. Rev.*, 2017, **117**, 7190-7239.

View Article Online
DOI: 10.1039/D1CP02928B

5. D. R. MacFarlane, N. Tachikawa, M. Forsyth, J. M. Pringle, P. C. Howlett, G. D. Elliott, J. H. Davis, M. Watanabe, P. Simon and C. A. Angell, *Energy Environ. Sci.*, 2014, **7**, 232-250.
6. H. Liu and H. Yu, *J. Mater. Sci. Technol.*, 2018, **35**, 674-686.
7. P. Sun and D. W. Armstrong, *Anal. Chem. Acta*, 2010, **661**, 1-16.
8. L. Brown, M. J. Earle, M. A. Gîlea, N. V. Plechkova and K. R. Seddon, in *Ionic Liquids II*, Springer 2017, pp. 85-125.
9. B. Soares, H. Passos, C. S. Freire, J. A. Coutinho, A. J. Silvestre and M. G. Freire, *Green Chem.*, 2016, **18**, 4582-4604.
10. C. F. Poole and N. Lenca, *J. Chromatogr. A*, 2014, **1357**, 87-109.
11. Suresh and J. S. Sandhu, *Green Chem. Lett. Rev.*, 2011, **4**, 289-310.
12. I. Newington, J. M. Perez-Arlandis and T. Welton, *Org. Lett.*, 2007, **9**, 5247-5250.
13. G. A. Baker, S. N. Baker, S. Pandey and F. V. Bright, *Analyst*, 2005, **130**, 800-808.
14. B. Prince, B. Fritz and Y. Chiu, *Ionic Liquids: Science and Applications*, 2012, **1117**, 27-49.
15. B. R. Donius and J. L. Rovey, *J. Spacecr. Rockets*, 2011, **48**, 110-123.
16. S. P. Berg and J. L. Rovey, *J. Propul. Power*, 2013, **29**, 339-351.
17. A. L. Patrick, *Rapid Commun. Mass Spectrom.*, 2020, **34**, e8587.
18. M. Yamashita and J. B. Fenn, *J. Phys. Chem.*, 1984, **88**, 4451-4459.
19. P. Lozano and M. Martinez-Sanchez, *J. Colloid Interface Sci.*, 2005, **282**, 415-421.
20. N. A. Mehta and D. A. Levin, *Aerospace*, 2018, **5**, 1-18.
21. N. Demmons, V. Hruby, D. Spence, T. Roy, E. Ehrbar, J. Zwahlen, R. Martin, J. Ziemer and T. Randolph, ST7-DRS Mission Colloid Thruster Development, 2008.
22. G. Anderson, J. Anderson, M. Anderson, G. Aveni, D. Bame, P. Barela, K. Blackman, A. Carmain, L. Chen and M. Cherng, *Phys. Rev. D*, 2018, **98**, 102005.
23. A. L. Patrick and C. J. Annesley, *J. Mass Spectrom.*, 2019, **54**, 371-377.
24. A. L. Patrick, K. M. Vogelhuber, B. D. Prince and C. J. Annesley, *J. Phys. Chem. A*, 2018, **122**, 1960-1966.
25. A. M. Fernandes, J. A. Coutinho and I. M. Marrucho, *J. Mass Spectrom.*, 2009, **44**, 144-150.
26. R. Bini, O. Bortolini, C. Chiappe, D. Pieraccini and T. Siciliano, *J. Phys. Chem. B*, 2007, **111**, 598-604.
27. F. C. Gozzo, L. S. Santos, R. Augusti, C. S. Consorti, J. Dupont and M. N. Eberlin, *Chem. Eur. J.*, 2004, **10**, 6187-6193.
28. J. Vitorino, J. P. Leal and M. E. Minas da Piedade, *ChemPhysChem*, 2015, **16**, 1969-1977.
29. A. M. Fernandes, M. A. Rocha, M. G. Freire, I. M. Marrucho, J. A. Coutinho and L. M. Santos, *J. Phys. Chem. B*, 2011, **115**, 4033-4041.
30. Y. Zhou, J. Zhan, X. Gao, C. Li, K. Chingin and Z. Le, *Can. J. Chem.*, 2014, **92**, 611-615.
31. O. Bortolini, C. Chiappe, T. Ghilardi, A. Massi and C. S. Pomelli, *J. Phys. Chem. A*, 2015, **119**, 5078-5087.
32. M. De Silva, A. C. Brown and A. L. Patrick, *J. Mass Spectrom.*, 2020, **55**, e4518.
33. P. A. Hunt, C. R. Ashworth and R. P. Matthews, *Chem. Soc. Rev.*, 2015, **44**, 1257-1288.
34. B. D. Prince, P. Tiruppathi, R. J. Bemish, Y.-H. Chiu and E. J. Maginn, *J. Phys. Chem. A*, 2015, **119**, 352-368.
35. C. J. Johnson, J. A. Fournier, C. T. Wolke and M. A. Johnson, *J. Chem. Phys.*, 2013, **139**, 224305.
36. J. A. Fournier, C. T. Wolke, C. J. Johnson, A. B. McCoy and M. A. Johnson, *J. Chem. Phys.*, 2015, **142**, 064306.
37. N. E. Heimer, R. E. Del Sesto, Z. Meng, J. S. Wilkes and W. R. Carper, *J. Mol. Liq.*, 2006, **124**, 84-95.
38. R. Holomb, A. Martinelli, I. Albinsson, J.-C. Lassegues, P. Johansson and P. Jacobsson, *J. Raman Spectrosc.*, 2008, **39**, 793-805.

View Article Online
DOI: 10.1039/D1CP02928B

39. T. Yamada, Y. Tominari, S. Tanaka and M. Mizuno, *J. Phys. Chem. B*, 2015, **119**, 15696-15705.
40. R. Cooper, A. M. Zolot, J. A. Boatz, D. P. Sporleder and J. A. Stearns, *J. Phys. Chem. A*, 2013, **117**, 12419-12428.
41. R. S. Booth, C. J. Annesley, J. W. Young, K. M. Vogelhuber, J. A. Boatz and J. A. Stearns, *Phys. Chem. Chem. Phys.*, 2016, **18**, 17037-17043.
42. J. M. Voss, B. M. Marsh, J. Zhou and E. Garand, *Phys. Chem. Chem. Phys.*, 2016, **18**, 18905-18913.
43. E. R. Talaty, S. Raja, V. J. Storhaug, A. Dölle and W. R. Carper, *J. Phys. Chem. B*, 2004, **108**, 13177-13184.
44. S. A. Katsyuba, E. E. Zvereva, A. Vidiš and P. J. Dyson, *J. Phys. Chem. A*, 2007, **111**, 352-370.
45. Y. Umebayashi, T. Fujimori, T. Sukizaki, M. Asada, K. Fujii, R. Kanzaki and S.-i. Ishiguro, *J. Phys. Chem. A*, 2005, **109**, 8976-8982.
46. S. Tsuzuki, H. Tokuda and M. Mikami, *Phys. Chem. Chem. Phys.*, 2007, **9**, 4780-4784.
47. K. Dong, S. Zhang, D. Wang and X. Yao, *J. Phys. Chem. A*, 2006, **110**, 9775-9782.
48. S. Kamalakannan, M. Prakash, M. M. Al-Mogren, G. Chambaud and M. Hochlaf, *J. Phys. Chem. C*, 2019, **123**, 15087-15098.
49. A. Thomas, K. R. Maiyelvaganan, S. Kamalakannan and M. Prakash, *ACS Omega*, 2019, **4**, 22655-22666.
50. J. Fuller, R. T. Carlin, H. C. De Long and D. Haworth, *J. Chem. Soc., Chem. Commun.*, 1994, 299-300.
51. T. Endo, H. Masu, K. Fujii, T. Morita, H. Seki, S. Sen and K. Nishikawa, *Cryst. Growth Des.*, 2013, **13**, 5383-5390.
52. A. R. Choudhury, N. Winterton, A. Steiner, A. I. Cooper and K. A. Johnson, *J. Am. Chem. Soc.*, 2005, **127**, 16792-16793.
53. S. M. Dibrov and J. K. Kochi, *Acta Crystallogr. C*, 2006, **62**, o19-o21.
54. H. A. Roy and M. T. Rodgers, *Phys. Chem. Chem. Phys.*, 2021, **23**, 13405-13418.
55. H. A. Roy, L. A. Hamlow and M. T. Rodgers, *J. Phys. Chem. A*, 2020, **124**, 10181-10198.
56. H. A. Roy and M. T. Rodgers, *J. Phys. Chem. A*, 2020, **124**, 10199-10215.
57. M. T. Rodgers, *J. Phys. Chem. A*, 2001, **105**, 2374-2383.
58. Y. Chen and M. T. Rodgers, *J. Am. Chem. Soc.*, 2012, **134**, 2313-2324.
59. R. Moision and P. Armentrout, *J. Am. Soc. Mass Spectrom.*, 2007, **18**, 1124–1134.
60. N. F. Dalleska, K. Honma and P. B. Armentrout, *J. Am. Chem. Soc.*, 1993, **115**, 12125-12131.
61. N. Aristov and P. B. Armentrout, *J. Phys. Chem.*, 1986, **90**, 5135-5140.
62. D. A. Hales and P. B. Armentrout, *J. Clust. Sci.*, 1990, **1**, 127-142.
63. N. R. Daly, *Rev. Sci. Instrum.*, 1960, **31**, 264-267.
64. M. J. Frisch, G. W. Trucks, H. B. Schlegel, G. E. Scuseria, M. A. Robb, J. R. Cheeseman, G. Scalmani, V. Barone, B. Mennucci and G. A. Petersson, et al., Gaussian, Inc., Wallingford, CT, revision C.01 edn., 2009.
65. A. D. Becke, *J. Chem. Phys.*, 1993, **98**, 5648-5652.
66. C. Lee, W. Yang and R. G. Parr, *Phys. Rev. B*, 1988, **37**, 785-789.
67. S. F. Sousa, P. A. Fernandes and M. J. Ramos, *J. Phys. Chem. A*, 2007, **111**, 10439-10452.
68. J. Tirado-Rives and W. L. Jorgensen, *J. Chem. Theory Comput.*, 2008, **4**, 297-306.
69. S. Grimme, S. Ehrlich and L. Goerigk, *J. Comput. Chem.*, 2011, **32**, 1456-1465.
70. Y. Zhao and D. G. Truhlar, *Theor. Chem. Acc.*, 2008, **120**, 215-241.
71. S. Simon, M. Duran and J. Dannenberg, *J. Chem. Phys.*, 1996, **105**, 11024-11031.
72. S. F. Boys and R. Bernardi, *Mol. Phys.*, 1970, **19**, 553-566.
73. J. P. Merrick, D. Moran and L. Radom, *J. Phys. Chem. A*, 2007, **111**, 11683–11700.
74. J. Contreras-García, E. R. Johnson, S. Keinan, R. Chaudret, J.-P. Piquemal, D. N. Beratan and W. Yang, *J. Chem. Theory Comput.*, 2011, **7**, 625-632.

View Article Online
DOI: 10.1039/D1CP02928B

75. E. R. Johnson, S. Keinan, P. Mori-Sánchez, J. Contreras-García, A. J. Cohen and W. Yang, *J. Am. Chem. Soc.*, 2010, **132**, 6498-6506.
76. W. Humphrey, A. Dalke and K. Schulten, *J. Mol. Graph.*, 1996, **14**, 33-38.
77. K. M. Ervin and P. B. Armentrout, *J. Chem. Phys.*, 1985, **83**, 166-189.
78. M. T. Rodgers, K. M. Ervin and P. B. Armentrout, *J. Chem. Phys.*, 1997, **106**, 4499-4508.
79. M. T. Rodgers and P. B. Armentrout, *J. Chem. Phys.*, 1998, **109**, 1787-1800.
80. T. S. Beyer and D. F. Swinehart, *Commun. ACM*, 1973, **16**, 379.
81. F. A. Khan, D. E. Clemmer, R. H. Schultz and P. B. Armentrout, *J. Phys. Chem.*, 1993, **97**, 7978-7987.
82. F. Muntean and P. Armentrout, *J. Phys. Chem. A*, 2003, **107**, 7413-7422.
83. F. Muntean and P. Armentrout, *Z. Phys. Chem.*, 2000, **214**, 1035-1064.
84. J. C. Amicangelo and P. B. Armentrout, *Int. J. Mass Spectrom.*, 2001, **212**, 301-325.
85. V. Romanov, C.-K. Siu, U. H. Verkerk, A. C. Hopkinson and K. M. Siu, *J. Phys. Chem. A*, 2010, **114**, 6964-6971.
86. Y. Chen and M. T. Rodgers, *Anal. Chem.*, 2012, **84**, 7570-7577.
87. Y. Chen and M. T. Rodgers, *J. Am. Chem. Soc.*, 2012, **134**, 5863-5875.
88. N. S. Rannulu and M. T. Rodgers, *J. Phys. Chem. A*, 2007, **111**, 3465-3479.
89. N. Hallowita, D. R. Carl, P. B. Armentrout and M. T. Rodgers, *J. Phys. Chem. A*, 2008, **112**, 7996–8008.
90. C. Ruan, Z. Yang and M. T. Rodgers, *Phys. Chem. Chem. Phys.*, 2007, **9**, 5902-5918.
91. N. S. Rannulu, R. Amunugama, Z. Yang and M. T. Rodgers, *J. Phys. Chem. A*, 2004, **108**, 6385-6396.
92. C. Ruan and M. T. Rodgers, *J. Am. Chem. Soc.*, 2004, **126**, 14600-14610.
93. H. Huang and M. T. Rodgers, *J. Phys. Chem. A*, 2002, **106**, 4277-4289.
94. M. T. Rodgers and P. B. Armentrout, *Int. J. Mass Spectrom.*, 1999, **185/186/187**, 359-380.
95. C. Ruan, Z. Yang, N. Hallowita and M. T. Rodgers, *J. Phys. Chem. A*, 2005, **109**, 11539-11550.

View Article Online
DOI: 10.1039/D1CP02928B

Table 1. Threshold Dissociation Energies at 0 K, Entropies of Activation at 1000 K, and Fitting Parameters of **eqn (4)** of $[C_{n-2}mim:PF_6:C_nmim]^+$ Clusters.[a]

System	Ionic Product	E_0(PSL)[b] (eV)	$\Delta S^{\ddagger}$ (PSL)[b] (J mol^{-1} K^{-1})	σ[b]	n[b]	E_0[c] (eV)	Kinetic Shift (eV)
$[C_2mim:PF_6:C_4mim]^+$	$[C_2mim]^+$	1.19 (0.05)	18 (5)	84.5 (4.9)	1.3 (0.1)	2.10 (0.08)	0.91
	$[C_4mim]^+$	1.15 (0.05)	17 (5)	84.5 (4.9)	1.3 (0.1)	2.00 (0.08)	0.84
$[C_4mim:PF_6:C_6mim]^+$	$[C_4mim]^+$	1.15_3 (0.05_6)	17 (4)	110.1 (4.0)	1.4 (0.1)	2.30 (0.10)	1.15
	$[C_6mim]^+$	1.14_9 (0.05_7)	24 (4)	56.9 (3.0)	1.4 (0.1)	2.27 (0.10)	1.12
$[C_6mim:PF_6:C_8mim]^+$	$[C_6mim]^+$	1.09 (0.07)	9 (4)	79.4 (13.2)	1.4 (0.2)	2.56 (0.10)	1.47
	$[C_8mim]^+$	1.07 (0.07)	5 (4)	79.4 (13.2)	1.4 (0.2)	2.44 (0.10)	1.38

[a]Present results based on competitive analyses of the CID product cross sections of **reactions 5** and **6** except as noted. Uncertainties are listed in parentheses. [b]Average values for loose a PSL TS. [c]Results based on analyses of the CID product cross sections using **eqn (2)**, without inclusion of lifetime or competitive effects.

Table 2. Enthalpies and Free Energies of Binding of the $[C_{n-2}mim:PF_6:C_nmim]^+$ Clusters at 298 K in kJ/mol[a]

System	Ionic Product	ΔH_0	ΔH_0[b]	$\Delta H_{298} - \Delta H_0$[b]	ΔH_{298}	ΔH_{298}[b]	$T\Delta S_{298}$[b]	ΔG_{298}	ΔG_{298}[b]
$[C_2mim:PF_6:C_4mim]^+$	$[C_2mim]^+$	114.8 (4.7)	115.4	-3.8 (0.1)	111.0 (4.7)	111.6	32.5 (1.5)	78.5 (4.9)	79.1
	$[C_4mim]^+$	111.3 (4.7)	111.0	-3.7 (0.1)	107.6 (4.7)	107.3	32.7 (1.5)	74.9 (4.9)	74.6
$[C_4mim:PF_6:C_6mim]^+$	$[C_4mim]^+$	111.2 (5.4)	107.8	-3.7 (0.1)	107.5 (5.4)	104.1	32.1 (1.5)	75.4 (5.6)	72.0
	$[C_6mim]^+$	110.9 (5.5)	110.9	-3.8 (0.1)	107.1 (5.5)	107.1	34.7 (1.5)	72.4 (5.7)	72.4
$[C_6mim:PF_6:C_8mim]^+$	$[C_6mim]^+$	105.4 (7.0)	108.2	-3.8 (0.1)	101.6 (7.0)	104.4	29.8 (1.5)	71.8 (7.2)	74.6
	$[C_8mim]^+$	102.8 (6.9)	106.8	-3.9 (0.1)	98.9 (6.9)	102.9	28.7 (1.5)	70.2 (7.1)	74.2

[a]Present results, uncertainties are listed in parentheses. [b]Values calculated at the B3LYP/6-311+G(2d,2p)//B3LYP/6-311+G(d,p) level of theory with frequencies scaled by 0.9887 and including BSSE corrections.

View Article Online
DOI: 10.1039/D1CP02928B

Table 3. Absolute Bond Dissociation Energies of $[C_{n-2}mim:PF_6:C_nmim]^+$ Clusters at 0 K in kJ/mol.[a]

System	Ionic Product	TCID	B3LYP[b]		B3LYP-GD3BJ[c]		M06-2X[d]	
			D_0	$D_{0,BSSE}$[e]	D_0	$D_{0,BSSE}$[e]	D_0	$D_{0,BSSE}$[e]
$[C_2mim:PF_6:C_4mim]^+$	$[C_2mim]^+$	114.8 (4.7)	120.8	115.4	130.3	123.2	131.3	121.7
	$[C_4mim]^+$	111.3 (4.7)	117.3	111.0	128.7	120.3	128.8	117.7
$[C_4mim:PF_6:C_6mim]^+$	$[C_4mim]^+$	111.2 (5.4)	113.3	107.8	130.6	122.2	127.8	116.6
	$[C_6mim]^+$	110.9 (5.5)	116.5	110.9	129.9	121.3	126.0	116.2
$[C_6mim:PF_6:C_8mim]^+$	$[C_6mim]^+$	105.4 (7.0)	113.9	108.2	137.9	127.9	122.2	112.5
	$[C_8mim]^+$	102.8 (6.9)	113.4	106.8	141.9	130.8	122.2	112.4
AEU/MAD[f]		5.7 (1.0)	6.5 (2.9)	1.9 (1.8)	23.8 (9.6)	14.9 (8.3)	17.0 (1.4)	6.8 (1.6)

[a]Present results, uncertainties are listed in parentheses. [b]Calculated at the B3LYP/6-311+G(2d,2p) level of theory using B3LYP/6-311+G(d,p) optimized geometries including ZPE corrections. [c]Calculated at the B3LYP-GD3BJ/6-311+G(2d,2p) level of theory using B3LYP-GD3BJ/6-311+G(d,p) optimized geometries including ZPE corrections. [d]Calculated at the M06-2X/6-311+G(2d,2p) level of theory using M06-2X/6-311+G(d,p) optimized geometries including ZPE corrections. [e]Also includes BSSE corrections. [f]Average experimental uncertainty (AEU) and mean absolute deviation (MADs) between measured TCID and calculated values.

Table 4. Relative BDEs of $[C_{n-2}mim:PF_6:C_nmim]^+$ Clusters and Relative IPEs of $(C_{n-2}mim:PF_6)$ vs. $(C_nmim:PF_6)$ Ion Pairs at 0 K in kJ/mol.[a]

System	ΔIPE	B3LYP[b]		B3LYP-GD3BJ[c]		M06-2X[d]	
		D_0	$D_{0,BSSE}$[e]	D_0	$D_{0,BSSE}$[e]	D_0	$D_{0,BSSE}$[e]
$[C_2mim:PF_6:C_4mim]^+$	3.5 (1.2)	3.5	4.4	1.6	2.9	2.5	4.0
		3.5	*3.7*	*1.6*	*2.1*	*2.1*	*3.7*
$[C_4mim:PF_6:C_6mim]^+$	0.4 (1.2)	-3.2	-3.1	0.7	0.9	1.8	0.4
		-3.1	*-2.2*	*0.6*	*1.5*	*1.8*	*2.4*
$[C_6mim:PF_6:C_8mim]^+$	2.6 (1.0)	0.5	1.4	-4.0	-2.9	0.0	0.1
		0.5	*0.6*	*-4.0*	*-1.3*	*0.0*	*0.3*
AEU/MAD[f]	1.1 (0.1)[g]	1.9 (1.8)	1.9 (1.4)	2.9 (3.3)	2.2 (2.9)	1.7 (0.8)	1.0 (1.3)
		1.9 (1.8)	*1.6 (1.2)*	*2.9 (3.3)*	*2.1 (1.5)*	*1.8 (0.7)*	*1.5 (1.1)*

[a]Present results, uncertainties are listed in parentheses. Values in italics font are computed from differences in the energies of the $(C_{n-2}mim:PF_6)$ and $(C_nmim:PF_6)$ ion pairs and their component ions. [b]Calculated at the B3LYP/6-311+G(2d,2p) level of theory using B3LYP/6-311+G(d,p) optimized geometries including ZPE corrections. [c]Calculated at the B3LYP-GD3BJ/6-311+G(2d,2p) level of theory using B3LYP-GD3BJ/6-311+G(d,p) optimized geometries including ZPE corrections. [d]Calculated at the M06-2X/6-311+G(2d,2p) level of theory using M06-2X/6-311+G(d,p) optimized geometries including ZPE corrections. [e]Also includes BSSE corrections. [f]Mean absolute deviation (MADs) between TCID measured and calculated values. [g]Average experimental uncertainty

View Article Online
DOI: 10.1039/D1CP02928B

(AEU). Values in standard font are computed from the energies of the $[C_{n-2}mim:PF_6:C_nmim]^+$ cluster and its CID products.

Table 5. Computed Ion-Pairing Energies of the ($C_n$mim:PF_6) Ion Pairs at 0 K in kJ/mol. [a]

System	B3LYP[b]		B3LYP-GD3BJ[c]		M06-2X[d]	
	D_0	$D_{0,BSSE}$[e]	D_0	$D_{0,BSSE}$[e]	D_0	$D_{0,BSSE}$[e]
(C_2mim:PF_6)	322.8	316.0	351.2	342.6	360.9	350.5
(C_4mim:PF_6)	319.3	312.3	349.6	340.5	358.5	346.8
(C_6mim:PF_6)	322.4	314.5	349.0	339.0	356.7	344.4
(C_8mim:PF_6)	321.9	313.9	353.0	340.3	356.7	344.1

[a]All values included ZPE corrections. [b]Calculated at the B3LYP/6-311+G(2d,2p) level of theory using B3LYP/6-311+G(d,p) optimized geometries. [c]Calculated at the B3LYP-GD3BJ/6-311+G(2d,2p) level of theory using B3LYP-GD3BJ/6-311+G(d,p) optimized geometries. [d]Calculated at the M06-2X/6-311+G(2d,2p) level of theory using M06-2X/6-311+G(d,p) optimized geometries. [e]Also includes BSSE corrections.

Table 6. Bond Dissociation Energies of the $[2C_n mim:PF_6]^+$ Clusters at 0 K in kJ/mol.[a]

System	TCID[b]	TCID[c] (Evaluated)	B3LYP[d]		B3LYP-GD3BJ[e]		M06-2X[f]	
			D_0	$D_{0,BSSE}$[g]	D_0	$D_{0,BSSE}$[g]	D_0	$D_{0,BSSE}$[g]
$[2C_2mim:PF_6]^+$	113.0 (4.4)	114.8 (0.9)	119.2	113.3	134.1	126.4	134.5	124.4
$[2C_4mim:PF_6]^+$	112.3 (5.2)	111.4 (0.9)	119.0	112.6	130.8	122.5	126.4	116.8
$[2C_6mim:PF_6]^+$	110.6 (6.6)	111.1 (0.9)	113.3	107.6	120.0	111.9	130.9	119.6
$[2C_8mim:PF_6]^+$	110.3 (5.0)	108.6 (0.9)	113.3	107.6	138.3	127.0	121.9	112.1
AEU/MAD[h]	5.3 (0.9)	0.9 (0.0)	4.7 (2.1)	1.6 (1.5)	19.3 (7.7)	10.4 (6.6)	16.9 (4.8)	6.7 (4.3)
			4.7 (2.2)	*1.8 (1.2)*	*19.3 (8.5)*	*10.5 (7.3)*	*17.0 (3.3)*	*6.8 (2.8)*

[a]Present results, uncertainties are listed in parentheses. [b]Values taken from **reference** 54. [c]Values determined from regression analysis of the absolute and relative TCID 0 K BDEs. [d]Calculated at the B3LYP/6-311+G(2d,2p) level of theory using B3LYP/6-311+G(d,p) optimized geometries including ZPE corrections. [e]Calculated at the B3LYP-GD3BJ/6-311+G(2d,2p) level of theory using B3LYP-GD3BJ/6-311+G(d,p) optimized geometries including ZPE corrections. [f]Calculated at the M06-2X/6-311+G(2d,2p) level of theory using M06-2X/6-311+G(d,p) optimized geometries including ZPE corrections. [g]Includes BSSE corrections. [h]Average experimental uncertainty (AEU) and mean absolute deviation (MADs) between TCID and calculated values. MADs based on the directly measured BDEs taken from **reference** 54 are indicated in standard font; evaluated BDEs are indicated in italics.

View Article Online
DOI: 10.1039/D1CP02928B

FIGURE CAPTIONS

Figure 1. Chemical structures of the 1-alkyl-3-methylimidazolium cations, $[C_n\text{mim}]^+$ for n = 2, 4, 6 and 8, and the $[PF_6]^-$ anion. The atom numbering of the cations is indicated.

Figure 2. Kinetic-energy-dependent cross sections for collision-induced dissociation of the $[C_{n-2}\text{mim:}PF_6\text{:}C_n\text{mim}]^+$ clusters (for n = 4, 6, and 8) with Xe as a function of collision energy in the center-of-mass frame (lower x-axis) and laboratory frame (upper x-axis). The data shown was acquired at a Xe pressure of ~ 0.2 mTorr. The dominant fragmentation pathway is the competitive loss of a neutral ion pair and detection of $[C_{n-2}\text{mim}]^+$ and $[C_n\text{mim}]^+$ cations labeled for each cluster. The minor sequential dissociation pathways observed are summarized in **Table S1** (ESI†).

Figure 3. Overlay and expanded views of the threshold regions of the CID cross sections of the $[C_{n-2}\text{mim:}PF_6\text{:}C_n\text{mim}]^+$ clusters, where n = 4, 6 and 8 as a function of the center-of-mass collision energy. The data shown were acquired at a Xe pressure of ~ 0.2 mTorr. The total CID cross sections (σ_{tot}) and the $[C_n\text{mim}]^+$ and $[C_{n-2}\text{mim}]^+$ primary CID product cross sections for each cluster are separately compared in the top, middle and bottom panels, respectively. A small systematic increase in the apparent thresholds with increasing size of the cluster cations is seen in the data.

Figure 4. B3LYP/6-311+G(d,p) optimized geometries of the ground conformers of the $[C_n\text{mim}]^+$ cations and $[PF_6]^-$ anion. Noncovalent interaction maps at an isosurface of 0.20 a.u. of the reduced electron density gradients determined using a 6-311+G(2d,2p) basis set have been superimposed on the optimized structures.

View Article Online
DOI: 10.1039/D1CP02928B

Figure 5. B3LYP/6-311+G(d,p) optimized geometries of the ground conformers of the ($C_n$mim:PF_6) ion pairs. Noncovalent interaction maps at an isosurface of 0.20 a.u. of the reduced electron density gradients determined using a 6-311+G(2d,2p) basis set have been superimposed on the optimized structures.

Figure 6. B3LYP/6-311+G(d,p) optimized geometries of the ground conformers of the $[C_{n-2}mim:PF_6:C_nmim]^+$ clusters. Noncovalent interaction maps at an isosurface of 0.20 a.u. of the reduced electron density gradients determined using a 6-311+G(2d,2p) basis set have been superimposed on the optimized structures.

Figure 7. Zero-pressure-extrapolated cross sections for the collision-induced dissociation of the $[C_{n-2}mim:PF_6:C_nmim]^+$ clusters for n = 4, 6, and 8 with Xe as a function of center-of-mass frame (lower x-axis) and laboratory frame (upper x-axis). The solid lines represent the best competitive fits to the experimental data using **eqn (4)** and convoluted over the neutral and ion kinetic energy distributions. The dashed lines represent the model cross sections in the absence of experimental kinetic energy broadening for reactants with an internal energy corresponding to 0 K.

Figure 8. Comparison of the B3LYP computed 0 K BDEs versus measured threshold dissociation energies of the $[C_{n-2}mim:PF_6:C_nmim]^+$ clusters for n = 4, 6, and 8 (in kJ/mol). All theoretical values include ZPE and BSSE corrections. The $[C_nmim]^+$ and $[C_{n-2}mim]^+$ primary product cations are indicated with closed and open symbols, respectively. The n–2:n values of each cluster are indicated. The diagonal line indicates values for which the calculated and measured values are equal.

Figure 9. Comparison of the B3LYP computed relative BDEs of the $[C_{n-2}mim:PF_6:C_nmim]^+$ clusters (for n = 4, 6 and 8) and relative IPEs of the ($C_n$mim:PF_6) ion pairs (for n = 2, 4, 6, and 8) vs. experimentally determined 0 K ΔBDEs of the $[C_{n-2}mim:PF_6:C_nmim]^+$ clusters (for n = 4, 6

View Article Online
DOI: 10.1039/D1CP02928B

and 8). All theoretical values include ZPE and BSSE corrections. The ΔIPEs and ΔBDEs are indicated with open and closed symbols, respectively. The *n*–2:*n* values of each cluster are indicated. The diagonal lines indicate values for which the calculated and measured values are equal.

Figure 10. Absolute BDEs of the $[2C_n\text{mim:}PF_6]^+$ clusters at 0 K (in kJ/mol) as a function of the $[C_n\text{mim}]^+$ cation (n = 2, 4, 6, and 8) determined directly and evaluated from combined results of the independent and competitive TCID measurements (top panel) are indicated with open and closed symbols, respectively. Relative BDEs of the $[C_{n-2}\text{mim:}PF_6\text{:}C_n\text{mim}]^+$ clusters at 0 K (in kJ/mol) as a function of the $[C_{n-2}\text{mim}]^+$ and $[C_n\text{mim}]^+$ cations (n = 4, 6, and 8) determined from competitive TCID measurements (bottom panel).

Figure 11. Comparison of the B3LYP computed vs. TCID measured 0 K BDEs of the $[2C_n\text{mim:}PF_6]^+$ clusters for n = 2, 4, 6, and 8 (in kJ/mol). All theoretical values include ZPE and BSSE corrections. Values derived from direct TCID measurements[54] and those determined from regression analyses using the direct and competitive TCID measurements are indicated with open and closed symbols, respectively. The diagonal lines indicate values for which the calculated and measured values are equal.

Figure 12. Comparison of the evaluated TCID 0 K BDEs for $[2C_n\text{mim:}PF_6]^+$ and $[2C_n\text{mim:}BF_4]^+$ clusters as a function of chain length, n = 2, 4, 6, and 8.

View Article Online
DOI: 10.1039/D1CP02928B

37

Figure 1.

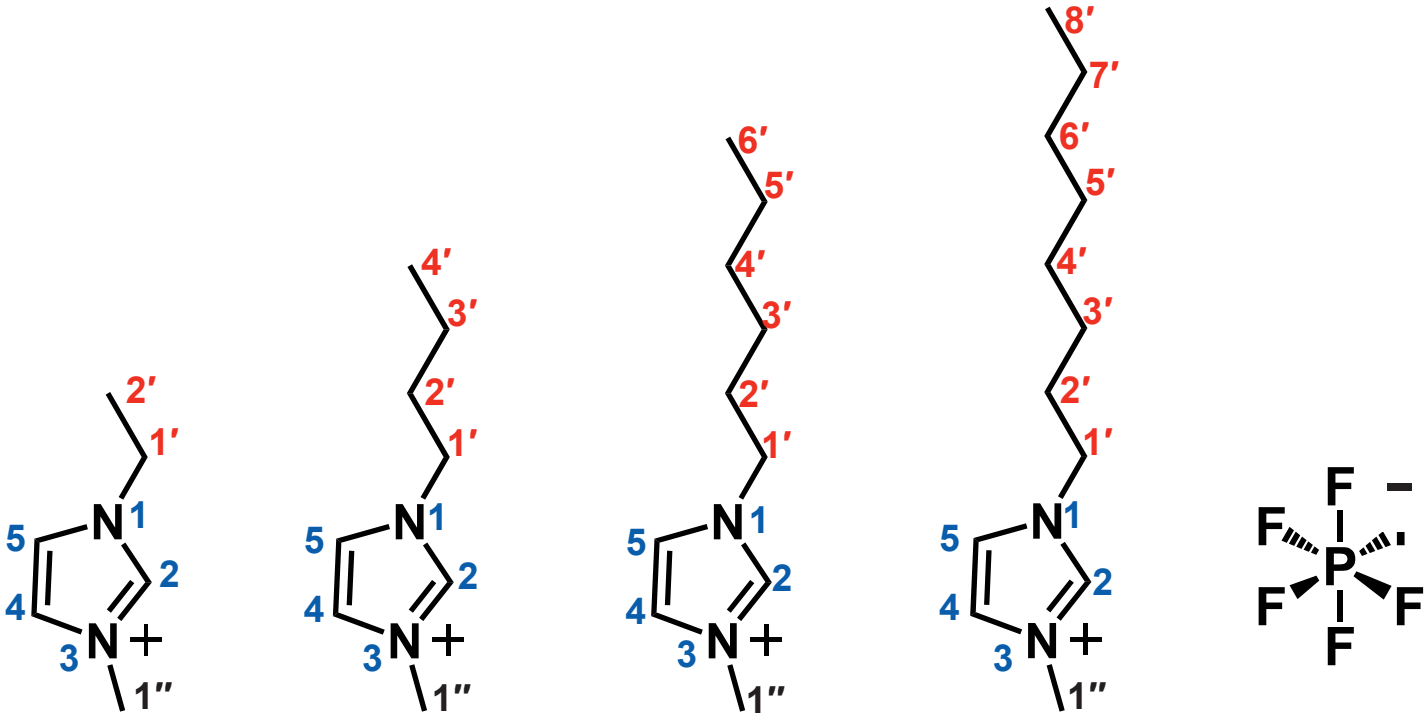

1-column figure, please reproduce at 50% of the current magnification

View Article Online
DOI: 10.1039/D1CP02928B

38

Figure 2.

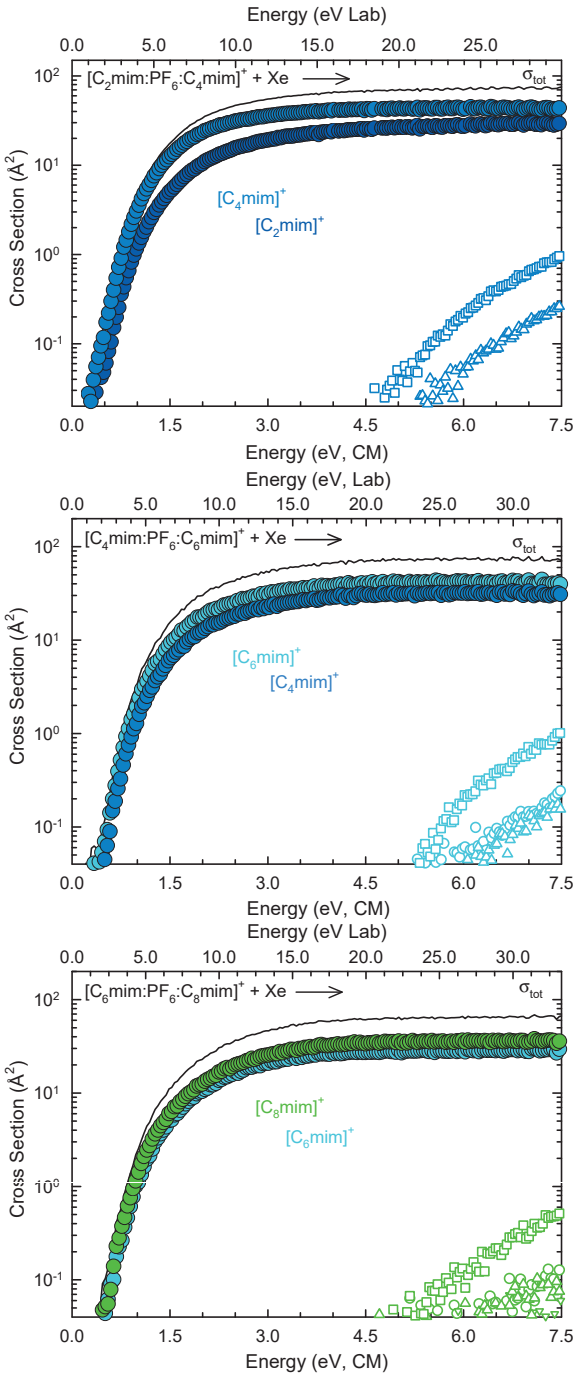

1-column figure, please reproduce at 100% of the current magnification

View Article Online
DOI: 10.1039/D1CP02928B

39

Figure 3.

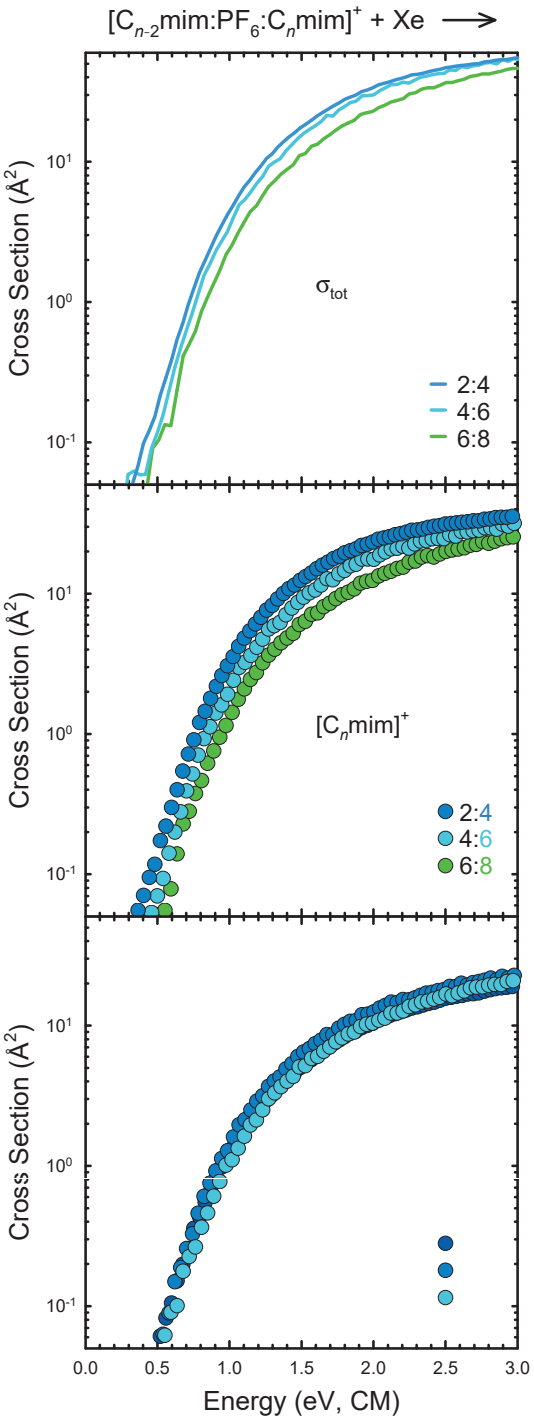

1-column figure, please reproduce at 100% of the current magnification

View Article Online
DOI: 10.1039/D1CP02928B

Figure 4.

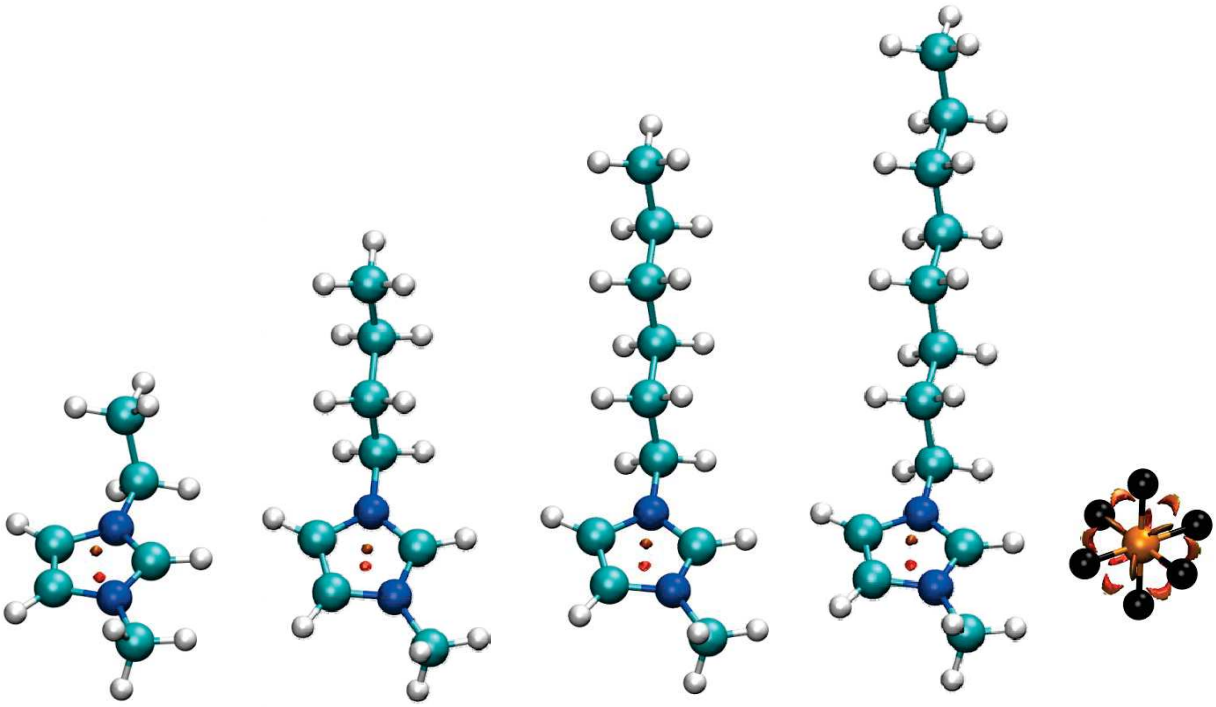

1-column figure, please reproduce at 50% of the current magnification

View Article Online
DOI: 10.1039/D1CP02928B

Figure 5.

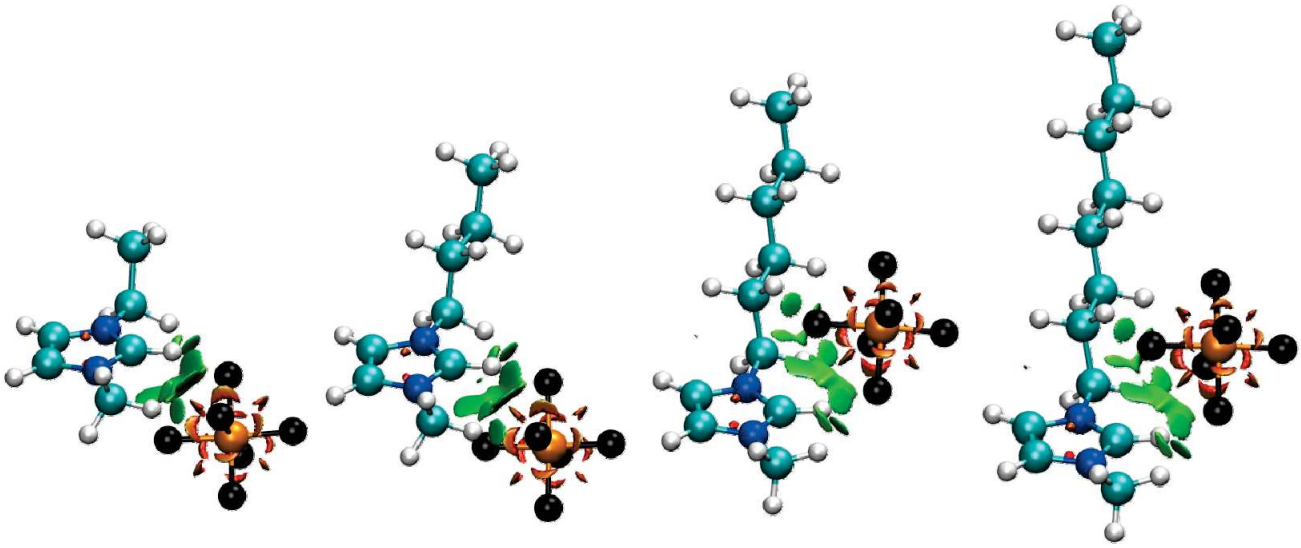

($\mathbf{g}_+\mathbf{F}$;g_-) (C_2mim:PF_6)

($\mathbf{g}_+\mathbf{F}$;g_-t_2) (C_4mim:PF_6)

($\mathbf{g}_-\mathbf{F}$;g_-t_4) (C_6mim:PF_6)

($\mathbf{g}_-\mathbf{F}$;g_-t_6) (C_8mim:PF_6)

1-column figure, please reproduce at 50% of the current magnification

View Article Online
DOI: 10.1039/D1CP02928B

Figure 6.

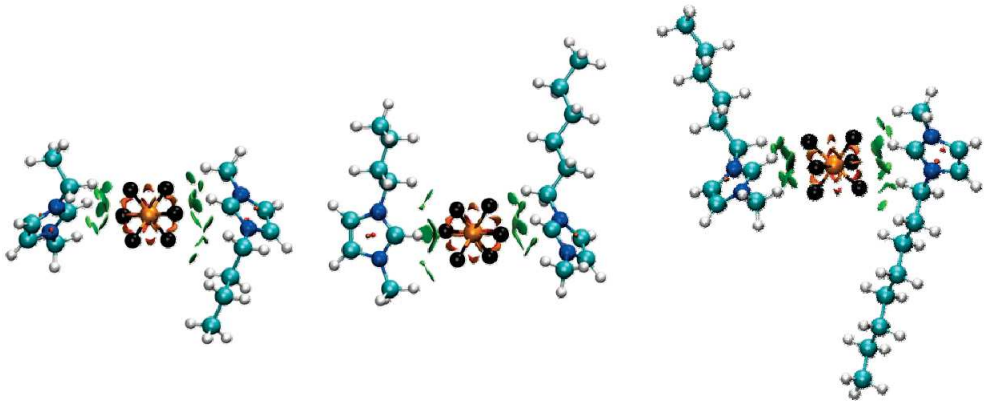

[g_;**g_cFcF**;g_t$_2$]$^+$
[C_2mim:PF_6:C_4mim]$^+$

[g_t$_2$;**g_cFcF**;g$_+$t$_4$]$^+$
[C_4mim:PF_6:C_6mim]$^+$

[g_t$_4$;**g_cFcF**;g_t$_6$]$^+$
[C_6mim:PF_6:C_8mim]$^+$

2-column figure, please reproduce at 100% of the current magnification

View Article Online
DOI: 10.1039/D1CP02928B

43

Figure 7.

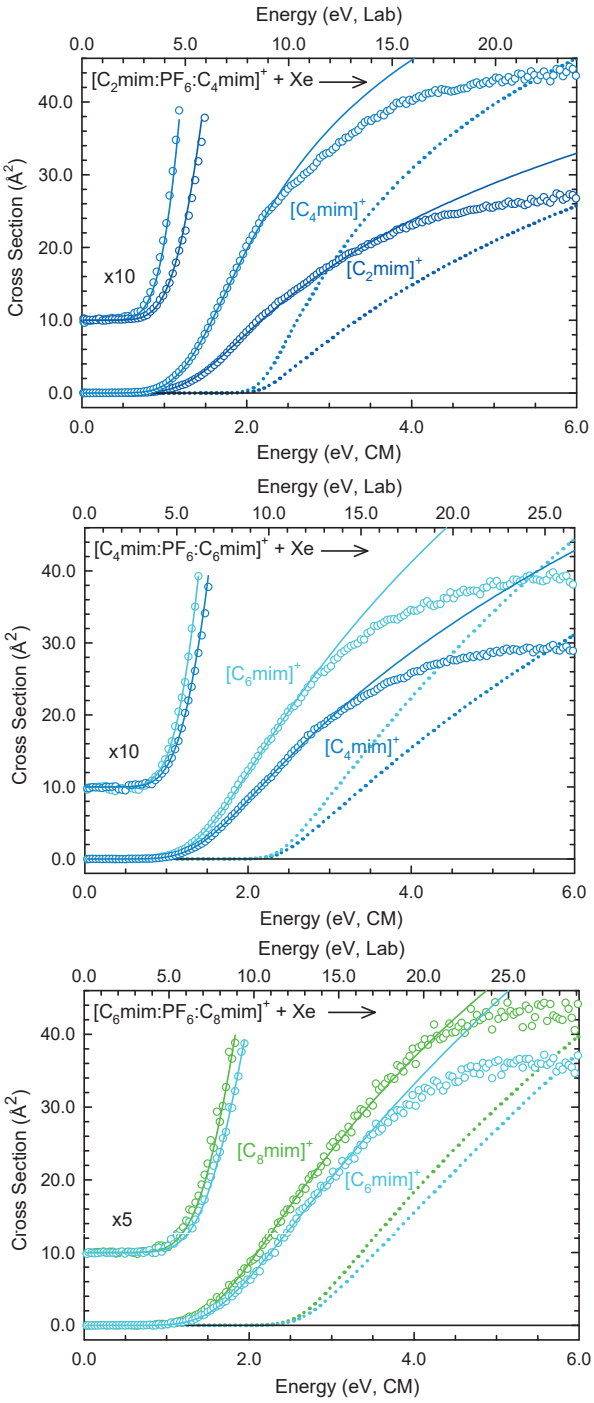

1-column figure, please reproduce at 100% of the current magnification

View Article Online
DOI: 10.1039/D1CP02928B

Figure 8.

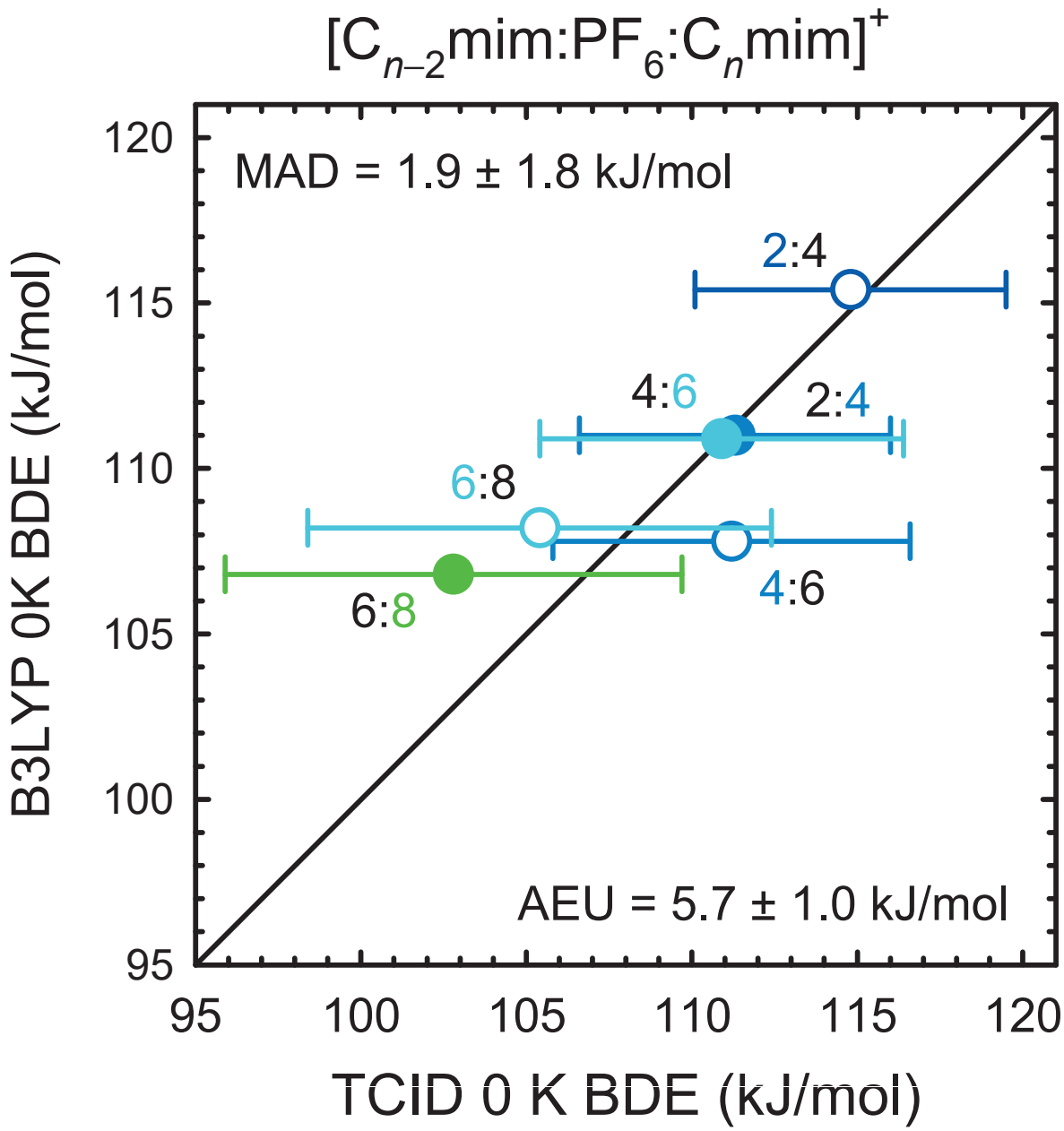

1-column figure, please reproduce at 50% of the current magnification

View Article Online
DOI: 10.1039/D1CP02928B

45

Figure 9.

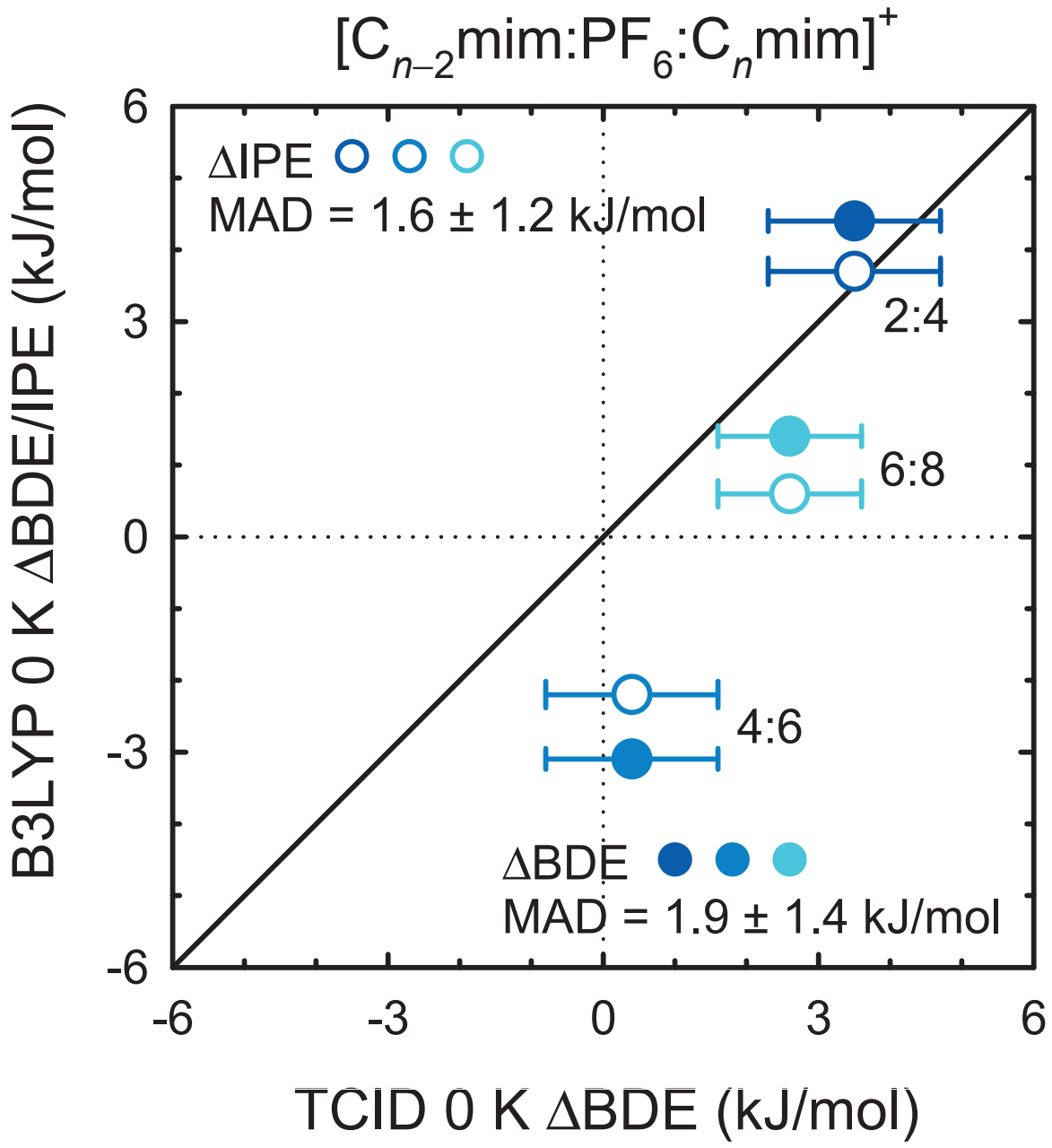

1-column figure, please reproduce at 50% of the current magnification

View Article Online
DOI: 10.1039/D1CP02928B

Figure 10.

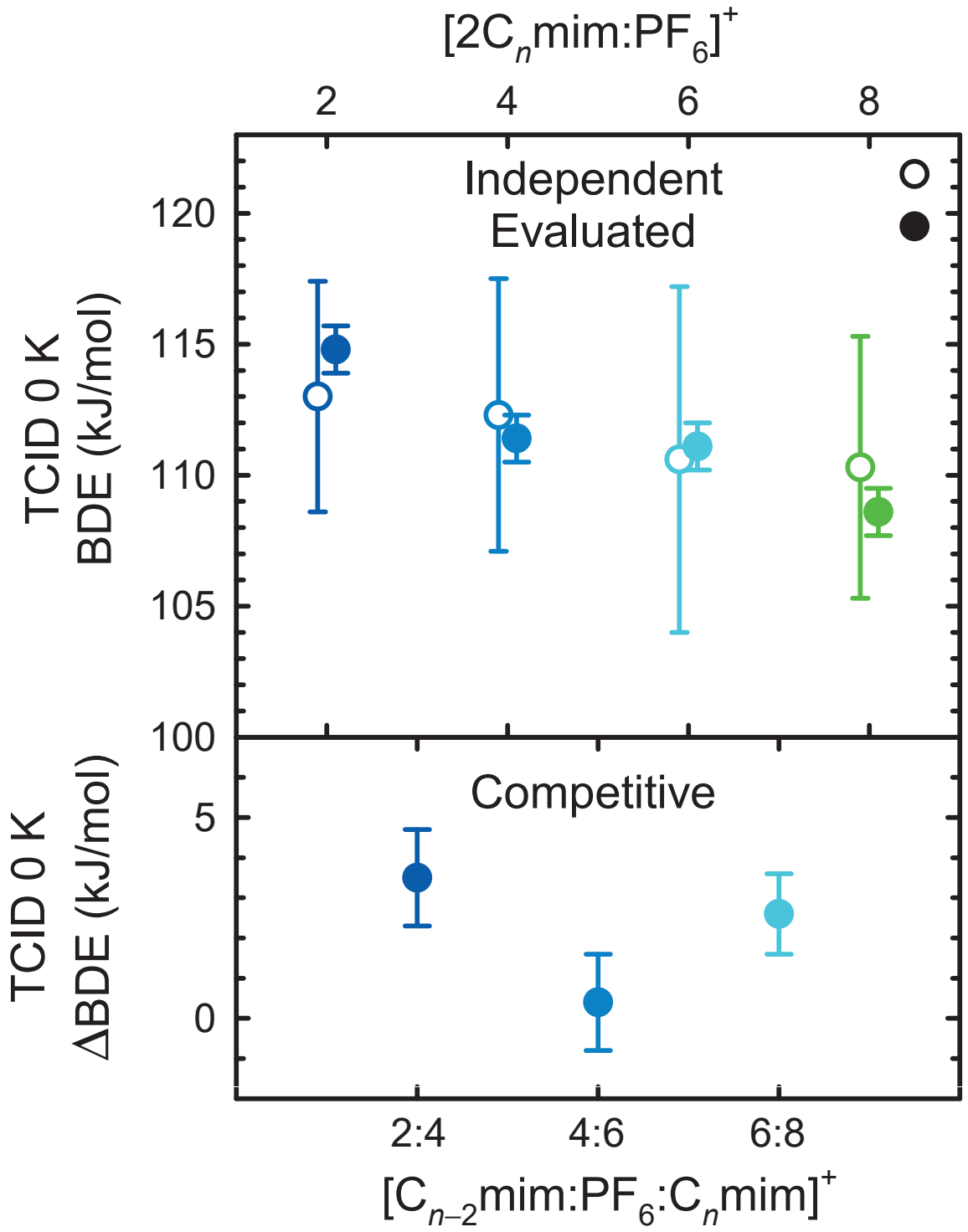

1-column figure, please reproduce at 50% of the current magnification

View Article Online
DOI: 10.1039/D1CP02928B

47

Figure 11.

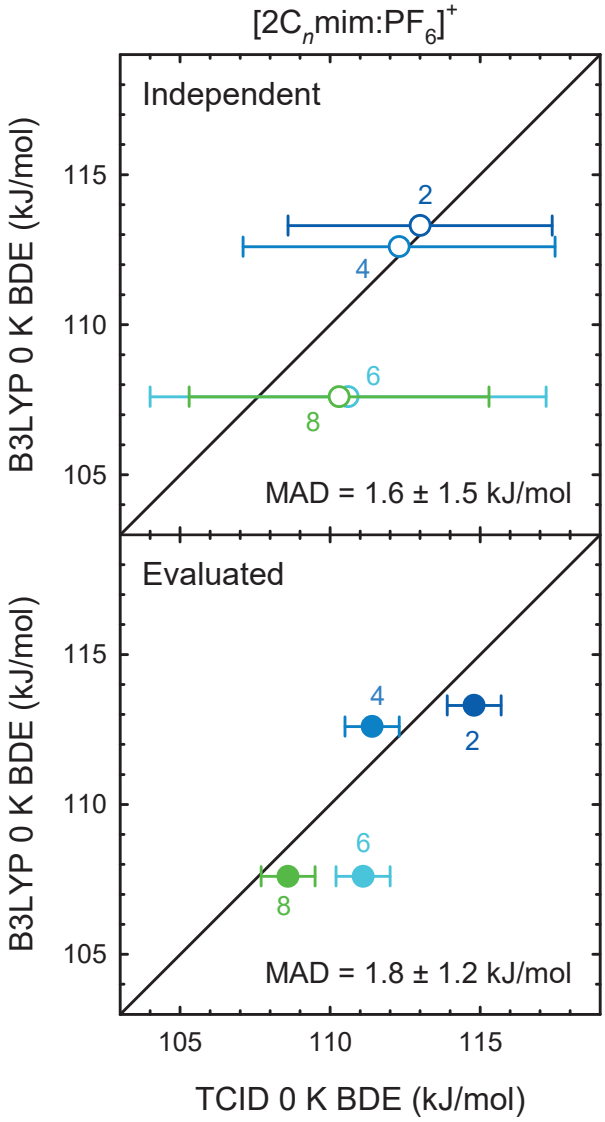

1-column figure, please reproduce at 100% of the current magnification

View Article Online
DOI: 10.1039/D1CP02928B

Figure 12.

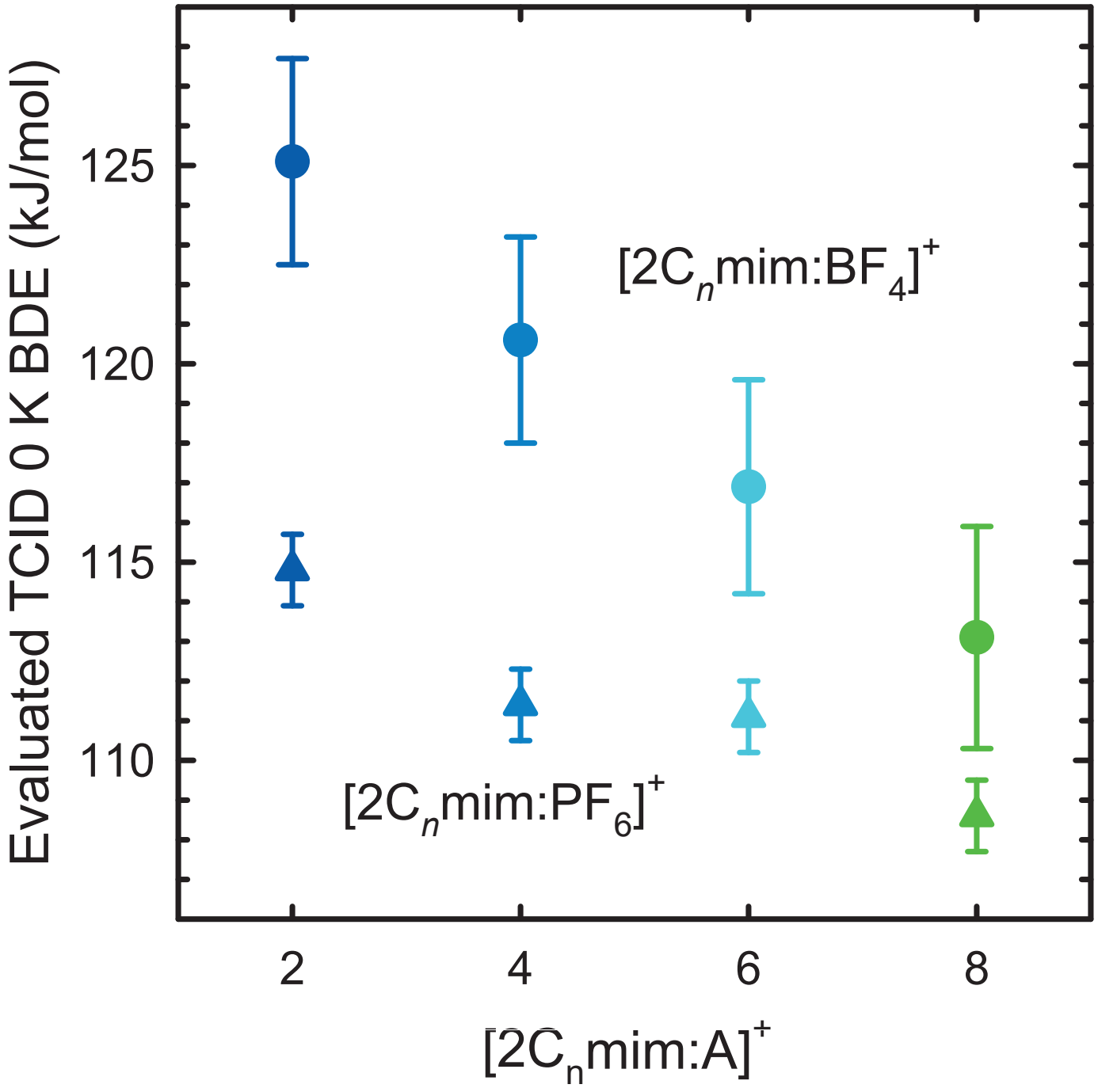

1-column figure, please reproduce at 50% of the current magnification